

First measurement of the bulk flow of nearby galaxies using the cosmic microwave background

Guilhem Lavaux^{1,2,3,4}, Niayesh Afshordi^{1,2}, Michael J. Hudson^{1,2}

¹ *Department of Physics & Astronomy, University of Waterloo, Waterloo, ON, N2L 3G1 Canada*

² *Perimeter Institute for Theoretical Physics, 31 Caroline St. N., Waterloo, ON N2L 2Y5, Canada*

³ *Department of Physics, University of Illinois at Urbana-Champaign, 1110 West Green Street, Urbana, IL 61801-3080*

⁴ *Department of Physics and Astronomy, The Johns Hopkins University, 3701 San Martin Drive, Baltimore, MD 21218, USA*

26 February 2024

ABSTRACT

Peculiar velocities in the nearby Universe can be measured via the kinetic Sunyaev-Zel’dovich (kSZ) effect. Using a statistical method based on an optimised cross-correlation with nearby galaxies, we extract the kSZ signal generated by plasma halo of galaxies from the Cosmic Microwave Background (CMB) temperature anisotropies observed by the Wilkinson Microwave Anisotropy Probe (WMAP). Marginalising over the thermal Sunyaev-Zel’dovich contribution from clusters of galaxies, possible unresolved point source contamination, and Galactic foregrounds, we find a kSZ bulk flow signal present at the $\sim 90\%$ confidence level in the seven-year WMAP data. When only galaxies within $50h^{-1}$ Mpc are included in the kSZ template we find a bulk flow in the CMB frame of $|V| = 533 \pm 263 \text{ km s}^{-1}$, in the direction $l = 324 \pm 27$, $b = -7 \pm 17$, consistent with bulk flow measurements on a similar scale using classical distance indicators. We show how this comparison constrains, for the first time, the (ionised) baryonic budget in the local universe. On very large ($\sim 500 h^{-1}$ Mpc) scales, we find a 95% upper limit of 470 km s^{-1} , inconsistent with some analyses of bulk flow of clusters from the kSZ. We estimate that the significance of the bulk flow signal may increase to $3\text{--}5\sigma$ using data from the PLANCK probe.

1 INTRODUCTION

Peculiar velocities are the only probe of the large-scale ($10 - 1000 h^{-1} \text{ Mpc}^1$) distribution of mass in the nearby Universe. Surveys of the peculiar velocity field have recently returned to spotlight, in part due to the availability of larger surveys of galaxy distances, such as the SFI++ (Masters et al. 2006) sample of Tully-Fisher distance or the “First Amendment” supernova compilation (Turnbull et al. 2012), as well as new analysis methods such as the minimum variance weighting method for bulk flows (Watkins et al. 2009) or the Monge-Ampère-Kantorovitch reconstruction (Lavaux et al. 2010). However, peculiar velocity surveys based on galaxy distances probe scales smaller than $\sim 100h^{-1}$ Mpc. The limitation is due to the linear increase of the peculiar velocity error with distance, and the cost of collecting the large samples that are necessary to statistically reduce this error. In contrast, the kinetic Sunyaev-Zel’dovich effect (Sunyaev & Zeldovich 1980, hereafter kSZ) is sensitive to relative motion of ionised gas with respect to the Cosmic Microwave Background (CMB). Therefore, as the kSZ errors do not

depend on distance, it is a promising probe of peculiar velocities on large scales.

Some recent peculiar velocity studies using classical distance indicators have suggested that there may be a cosmic bulk flow on scales of $\sim 50 - 100 h^{-1}$ Mpc in excess of that expected in Λ CDM (Watkins et al. 2009; Lavaux et al. 2010; Feldman et al. 2010; Colin et al. 2011), whereas other studies have found lower values (Nusser & Davis 2011; Turnbull et al. 2012). Clearly, it would be useful to have an independent probe of the peculiar velocity field on these scales.

On much larger scales, the kSZ effect in rich clusters has recently been used to measure the bulk flow by Kashlinsky et al. (2008, hereafter KAKE), following (Kashlinsky & Atrio-Barandela 2000). However, subsequent studies using similar data sets (Keisler 2009; Osborne et al. 2011; Mody & Hajian 2012) have not confirmed a flow with statistical significance claimed by KAKE. While the results of the latter authors have in turn been questioned (Atrio-Barandela et al. 2010; Kashlinsky et al. 2011, 2012), the lack of independent confirmation means that this very-large scale “Dark Flow” remains controversial. The main challenge is to disentangle the kSZ signal from the primary fluctuations of the CMB and the instrumental noise. The kSZ signal is at the level of a few μK ,

¹ The parameter h is today’s Hubble constant in units of $100 \text{ km s}^{-1} \text{ Mpc}^{-1}$.

while the CMB is in tens of μK and the noise may be in hundreds of μK for WMAP (Jarosik et al. 2011). Previous kSZ work has focused on clusters of galaxies (Haehnelt & Tegmark 1996; Kashlinsky et al. 2008; Osborne et al. 2011; Mody & Hajian 2012) because clusters hold a significant fraction (but not most) of the ionised plasma in the local universe. Indeed recently Hand et al. (2012) have detected the signal of pairwise infall of clusters using the kSZ effect. Unfortunately there are relatively few clusters of galaxies within $100\text{--}200h^{-1}$ Mpc in the nearby Universe, and so, as shown by the studies cited above, the corresponding errors on the bulk flow are large.

In this paper, we use galaxies themselves to produce a kSZ template which we cross-correlate with the CMB fluctuations. Galaxies, including spirals, are expected to have a large plasma halo (Fukugita & Peebles 2006; Rasmussen et al. 2009), indeed this is a standard assumption of galaxy formation models for over 40 years (Rees & Ostriker 1977; Silk 1977; White & Rees 1978). While much of the hot gas is expected to lie outside haloes, in the so-called warm-hot intergalactic medium (WHIM, Davé et al. 2001; Shull et al. 2011), nevertheless, this WHIM gas should be correlated with the haloes of larger galaxies and thus may be detected statistically through cross-correlations (see Softan 2006, for a claimed detection). In the context of this paper, therefore, “plasma halo” refers to both the hot plasma in the dark matter halo as well as plasma in the WHIM that is correlated with the galaxy.

The use of galaxies as kSZ tracers has also been advocated by Ho et al. (2009) and Shao et al. (2011). In particular, using 2MASS galaxies as a probe of the KAKE bulk flow has been proposed by Zhang (2010). On the one hand, in a given volume there are far more galaxies than there are clusters of galaxies, e.g., within $200h^{-1}$ Mpc, there are $\sim 60\,000$ galaxies in the 2M++ galaxy catalogue (Lavaux & Hudson 2011), whereas in the Reflex-eBCS-CIZA catalogue (RBC, Kocevski & Ebeling 2006), there are only 273 clusters of galaxies in the same volume. On the other hand, the density profile of the plasma halo is far more uncertain for galaxies than for the clusters of galaxies. Moreover, the plasma halo occupies a much smaller area on the sky, which requires an accurate modelling of beaming effects. Nevertheless there are expected to be more ionised electrons in or near galaxies than in clusters of galaxies, so smaller errors are expected from a galaxy sample.

The basic method used in this paper is to model the observed WMAP maps in all frequencies simultaneously using a combination of foreground templates to represent the kSZ effect as well as the thermal Sunyaev-Zeldovich (tSZ) effect. We also model the contamination from radio point sources that may be present in the galaxies, as well as Galactic foregrounds. We then analytically marginalise all results with respect to primary CMB fluctuations, and additionally marginalise over independent monopoles and dipoles in each channel.

In Section 2, we describe the statistical method used to fit the templates. In Section 3, we describe the data and models used to build the templates for the thermal and kinetic Sunyaev-Zel’dovich effects and point source contamination. In Section 4, we present and discuss our measurement of the kSZ effect. We compare the kSZ bulk

flow with results using other methods and measure the baryon fraction in free electrons in Section 5. In Section 6, we discuss future improvements and forecast the errors on the components of the kSZ bulk flow from the upcoming PLANCK temperature maps. Finally, Section 7 concludes the paper.

2 STATISTICAL METHOD

Here, we adopt a full-sky, multi-channel statistical model for WMAP7 data. We can model the observed sky temperature as a combination of multiple physical effects using a template based method, as in e.g. (Gorski et al. 1996; Jaffe et al. 2006). The templates that we consider in this work will model the two Sunyaev-Zel’dovich effects, the Point Source contaminations, the Galactic foreground emission, the residual temperature monopoles and dipoles. Generically, the expected observed signal d_c , in the frequency channel c , may be written as:

$$d_c = B_c \left(s + \sum_i \alpha_{i,\sigma_i(c)} t_{i,c} \right) + n, \quad (1)$$

where B_c is the beam of the instrument corresponding to channel c , n is an instrumental noise component, s is the Cosmic Microwave Background (CMB) signal, $\alpha_{i,\rho}$ are real scalars and $t_{i,c}$ is the template of signal i in the channel c (without beam). We note that B_c is a matrix operation, which can include convolution by any kind of smoothing kernel modelling the instrument response, provided the response is linear. $\sigma_i(c)$ expresses our prior on the frequency dependence for the physical signal i . In the case where the frequency dependence is not known, the operator is the identity, $\sigma_i(c) = c$. This implicitly states that for the template i , we have a number of free parameters corresponding to the number of frequency channels. In the case where the frequency dependence of the phenomenon i is known, $\sigma_i(c)$ does not depend on c , e.g. $\sigma_i(c) = 0$. This states that only one free parameter is required for all channels, e.g. $\alpha_{i,0}$. There may be other intermediate cases if some channels are at the same frequency. We may pick two concrete example that concern us in this work: the tSZ signal and the unresolved point source contamination map. In the case of tSZ, we know the frequency dependence, which is encoded in $t_{\text{tSZ},c}$. We thus only need one parameter α_{tSZ} . In the case of the map of point sources, the frequency dependence is unclear so we are leaving it free. We will have three parameters: $\alpha_{\text{PSC},Q}$, $\alpha_{\text{PSC},V}$, $\alpha_{\text{PSC},W}$.

We assume that the primary CMB signal is a realisation of a Gaussian random field, and that the instrumental noise is also Gaussian. After marginalisation over the primary CMB fluctuations, we may write the total log-likelihood as (see Appendix A):

$$\chi^2(\{\alpha_{i,\rho}\}) = \sum_{c,c'} (d_c - \sum_i \alpha_{i,\sigma_i(c)} B_c t_{i,c})^\dagger C_{c,c'}^{-1} (d_{c'} - \sum_i \alpha_{i,\sigma_i(c')} B_{c'} t_{i,c'}), \quad (2)$$

with

$$C_{c,c'}^{-1} = \tilde{N}_c^{-1} \mathbf{1}_{\delta_{c,c'}} - \tilde{N}_c^{-1} B_c S^{1/2} D^{-1} S^{1/2} B_{c'} \tilde{N}_{c'}^{-1}, \quad (3)$$

and

$$\mathbf{D} = \mathbf{1} + \mathbf{S}^{1/2} \left(\sum_{c''} \mathbf{B}_{c''} \tilde{\mathbf{N}}_{c''}^{-1} \mathbf{B}_{c''} \right) \mathbf{S}^{1/2}. \quad (4)$$

In the above, c and c' run over the available channels of WMAP, \mathbf{N}_c is the instrumental noise covariance matrix in the channel c . The inverse covariance matrix \mathbf{C}^{-1} does not use the noise covariance matrix (only its inverse) and it uses the angular CMB spectrum (and not its inverse). Thus, we do not have to worry about how to regulate the inverse of these two operators. In the above, we have used pseudo-inversion and we have set

$$\tilde{\mathbf{N}}_c^{-1} = \mathbf{M} \mathbf{N}_c^{-1} \mathbf{M}, \quad (5)$$

with \mathbf{M} the pixel masking operator. In the case of WMAP observations, we assume that the noise covariance matrix is diagonal in pixel space, but we do not assume homogeneity of the noise. It takes the form $\mathbf{N}_c^{-1} = N_{\text{obs},c} / \sigma_c^2$, with σ_c the noise normalisation and $N_{\text{obs},c}$ the number of observations for each frequency channels as provided by the WMAP collaboration. The matrix \mathbf{M} is an additional masking operation acting in pixel space. All pixels which are masked are set to zero by this operator. In our case, the mask will correspond to a HEALPIX map, with value either one, for accepting the pixel, or zero, for rejecting it. This form has already been used in Wandelt et al. (2004) in the context of Gibbs sampling of the CMB fluctuations.

If we assume that the angular power spectrum of the primary CMB is kept fixed, the equation (2) leads to an analytic solution of the $\alpha_{i,\rho}$:

$$\alpha_{i,\rho} = \sum_{j,\nu} \mathbf{A}_{(i,\rho),(j,\nu)}^{-1} \left(\sum_{\sigma_j(c)=\nu} \sum_{c'} \mathbf{t}_{j,c}^\dagger \mathbf{B}_{c'} \mathbf{C}_{c,c'}^{-1} \mathbf{d}_{c'} \right) \quad (6)$$

with

$$\mathbf{A}_{(i,\rho),(j,\nu)} = \sum_{\substack{c,c' \\ \sigma_i(c)=\rho, \sigma_j(c')=\nu}} \mathbf{t}_{i,c}^\dagger \mathbf{B}_c \mathbf{C}_{c,c'}^{-1} \mathbf{B}_{c'} \mathbf{t}_{j,c'}. \quad (7)$$

Computing $\mathbf{A}_{(i,\rho),(j,\nu)}$ requires applying $\mathcal{O}(N_t \times N_c)$ times the operator \mathbf{C}^{-1} . In this paper, we consider ten templates, and for one map per channel, three input maps. This results in applying \mathbf{C}^{-1} thirty times. We do not require more because, for a fixed primary CMB spectrum, we may precompute a weighted template $\tilde{\mathbf{t}}_{k,c}$, which is sufficient to compute all the terms of the covariance matrix \mathbf{A} and the maximum likelihood estimate α . The procedure is detailed in Appendix B.

For the practical purpose of the numerical implementation, we have separated the fitting of the Galactic foreground templates from the fluctuations due to kSZ, tSZ and point sources contamination. Doing so, the matrix \mathbf{A} , with 21×21 elements, stays the same for all of our experiments on the SZ components and point sources. We have separated the fitting using Gibbs sampling on a set of parameters $\alpha_{i,\rho}$ assuming the other set is fixed. Gibbs sampling provides samples of the posterior distributions. On the positive side, by selecting samples, we can impose a non-Gaussian prior on the $\{\alpha_{i,\rho}\}$. On the negative side, we are required to run a sampling chain. If

the templates are correlated, this chain may take time to converge. In practice though, for the cases of Section 4, the convergence is achieved in a few steps.

3 TEMPLATE GENERATION

In this section, we describe the physical models used to generate the templates of the three signals considered in this work: kinetic Sunyaev-Zel'dovich (kSZ), the thermal Sunyaev-Zel'dovich (tSZ) and radio point source contamination (PSC).

The signal from the kinetic Sunyaev-Zel'dovich effect is our primary goal. This is derived from the galaxies belonging to 2M++ galaxy compilation (Lavaux & Hudson 2011), which in turn is based on the 2MASS eXtended Sources Catalog (Skrutskie et al. 2006) and publicly-available redshift surveys.

The thermal Sunyaev-Zel'dovich (tSZ) signal is produced mostly by clusters of galaxies. As clusters and galaxies are correlated, it is necessary to also model the tSZ signal and marginalise over it. We model the signal using the position and luminosity of clusters in the RBC (Kocevski & Ebeling 2006) catalogue.

Finally, it may be expected that a subset of local galaxies host radio or submillimetre sources that contaminate WMAP data as unresolved point sources. The population of galaxies and of unresolved point sources may thus be correlated and must also be marginalised over. The contamination by unresolved point sources is obtained using the information contained in the 2MASS eXtended Sources Catalog (Skrutskie et al. 2006, hereafter 2MASS-XSC).

For fitting the contamination of the temperature fluctuations due to Milky-Way emission, we have used the templates provided by the WMAP7 collaboration on LAMBDA.² We have fitted the templates at the full resolution of $N_{\text{side}} = 512$.

We now describe the templates in detail.

3.1 kSZ model

We assume there is a massive halo of ionised plasma around galaxies. Fukugita & Peebles (2006) proposed an isothermal model for this plasma halo, which we further modify by introducing a hole at the centre of the galaxy. There are at least two reasons to do this. First, we reduce the possibility of correlating the kSZ signal with radio sources located at the centres of galaxies. Second, we expect that the plasma close to the centre of the haloes would cool and collapse to form the cold gas and stars in galaxies. Thus we adopt the following model:

$$\rho_g(r) = \begin{cases} \frac{\Omega_b}{\Omega_M} \frac{\sigma^2}{2\pi G} \frac{1}{r^2} & \text{if } R_g < r < R_v, \\ 0 & \text{otherwise,} \end{cases} \quad (8)$$

with R_v the maximum extent of our gas profile, and $R_g = 15h^{-1}$ kpc. In doing so, we do not attempt to fit

² The templates are located at http://lambda.gsfc.nasa.gov/product/map/dr4/templates_get.cfm.

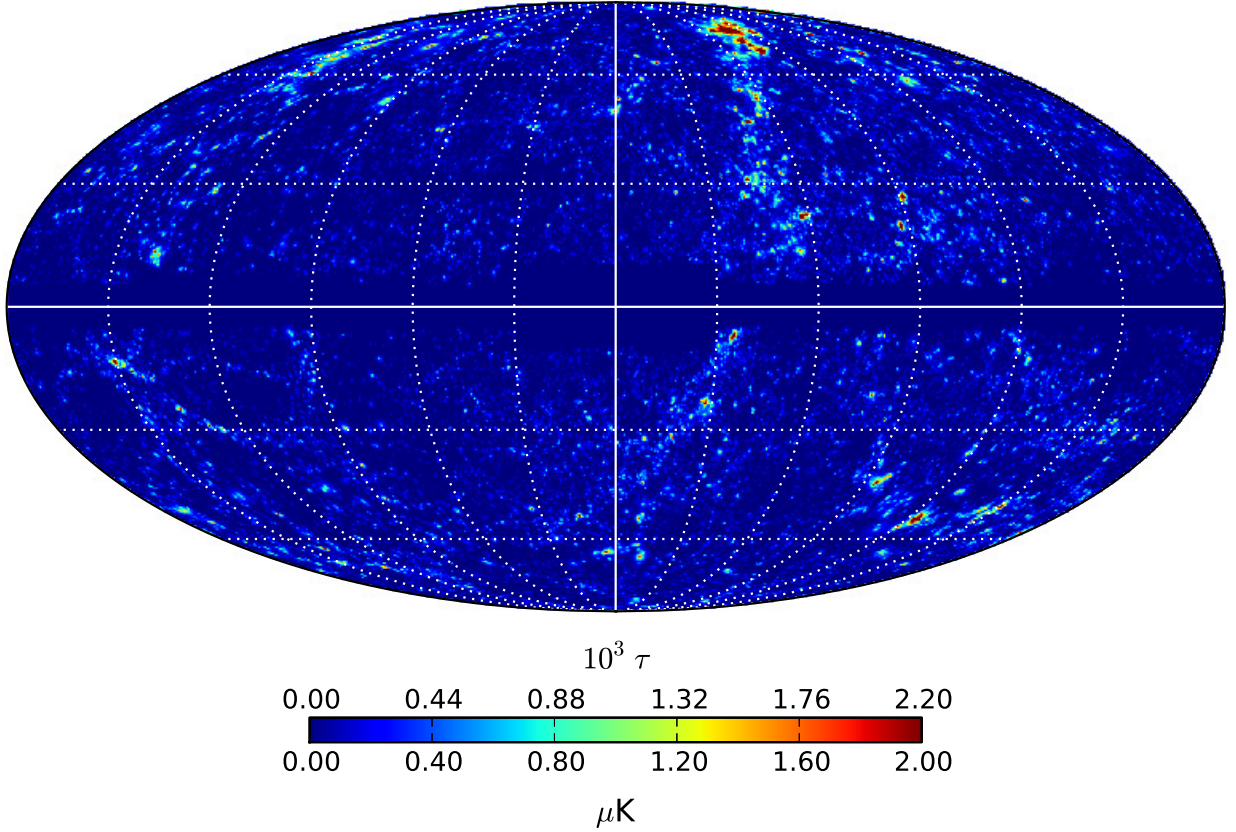


Figure 1. A map of the expected kSZ signal assuming each galaxy has an inward peculiar velocity of 100 km s^{-1} , before smoothing with the beam. Only galaxies with $cz \leq 20,000 \text{ km s}^{-1}$ have been included for generating this template. The grid lines are separated by 30° in the longitude and the latitude directions. The color scale also indicates the corresponding optical depth in unit of 10^3 .

the part of the galaxy dominated by stars and may avoid some point source contamination. The density of electrons is determined from the gas density, and the Helium abundance Y

$$n_e(r) = \frac{1}{m_p} \left(1 - \frac{Y}{2}\right) \rho_g(r), \quad (9)$$

with m_p the mass of the proton, and ρ_g the total mass density of the gas, and $Y = 0.245$ (e.g. Komatsu et al. 2011).

The kSZ effect depends on the electron density and the velocity of the electrons with respect to the primary CMB, i.e. it is proportional to the momentum. The velocity of a galaxy in the 2M++ sample can be modelled using linear perturbation theory applied to the density field. Here instead, for simplicity, we model the flow field to lowest order, i.e. by a dipole or “bulk flow” with constant Cartesian components V_i . The average kSZ temper-

ature change due to a bulk flow is given by:

$$\Delta T_{\text{kSZ}}(\hat{n}) = -2 T_{\text{CMB}} \sigma_T \left(\int_0^{\sqrt{(R_v)^2 - r_c^2(\hat{n})}} n_e \left[\sqrt{s^2 + r_c^2(\hat{n})} \right] ds \right) \left(\sum_{i=1}^3 \frac{V_i}{c} \hat{n}_i \right), \quad (10)$$

with r_c is given by Equation (12). After integration, we get:

$$\Delta T_{\text{kSZ}}(\hat{n}) = -\frac{\Omega_b}{\Omega_M} \frac{T_{\text{CMB}} \sigma_T f_e \sigma^2}{\pi G \mu_e m_p c} \frac{1}{D_A} \tan^{-1} \left(\sqrt{\frac{R_v^2}{r_c^2(\hat{n})} - 1} \right) \left(\sum_{i=1}^3 V_i \hat{n}_i \right) \Theta(r_c(\hat{n}) - R_g), \quad (11)$$

with Θ the Heaviside step function, f_e being the fraction of free electrons, $\mu_e = 2/(2 - Y) \simeq 1.14$, and $\sigma = 160 \text{ km s}^{-1}$ the typical velocity dispersion of galactic haloes. r_c is the projected distance from the centre of the

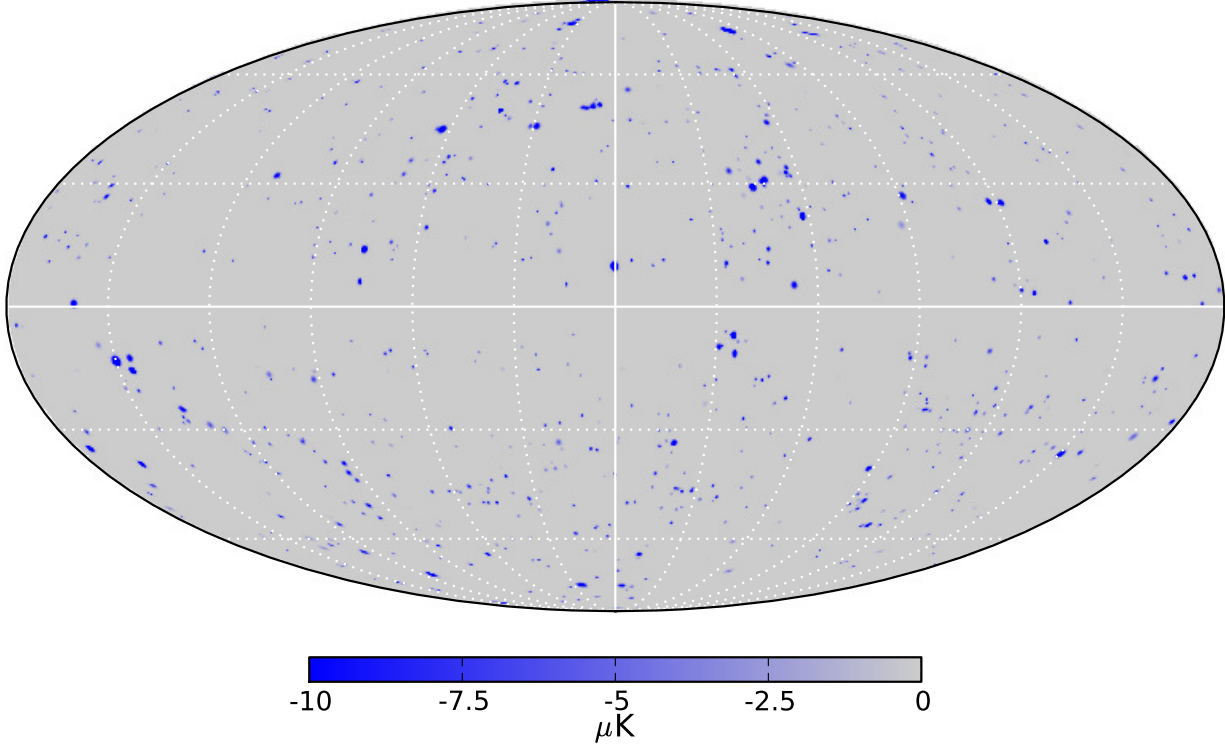


Figure 2. A map of the template for the tSZ signal in the W channel of WMAP, before smoothing with the beam. We use a resolution of $N_{\text{side}} = 1024$.

galaxy:

$$r_c(\hat{n}) = D_A(z_c) \sin [\cos^{-1}(\hat{n} \cdot \hat{n}_c)] = D_A(z_c) \sqrt{1 - (\hat{n} \cdot \hat{n}_c)^2} \quad (12)$$

where $D_A(z_c)$ is the angular distance of the galaxy at redshift z_c , and \hat{n}_c is the unit vector in the direction of the galaxy. We set the kSZ template to zero at small radii $r_c(\hat{n}) < R_g$. Finally, we scale R_v according to the luminosity as:

$$R_v = m_v \frac{\sigma}{\sqrt{50} H_0} \left(\frac{L_K}{L_*} \right)^{1/3} \simeq (220 h^{-1} \text{ kpc}) m_v \left(\frac{L_K}{L_*} \right)^{1/3}, \quad (13)$$

with $L_* = 3.8 \times 10^{10} h^{-2} L_\odot$ as given for the best Schechter function fit in Lavaux & Hudson (2011). We take the normalisation from Fukugita & Peebles (2006). The parameter m_v is introduced to increase the effective radius of the plasma halo. As noted above the “plasma halo” refers not only to the actual halo of a given galaxy but also to all correlated plasma. The choice of m_v is selected so that all free electrons, including those in the WHIM or associated with low luminosity galaxies not in the 2M++ catalogue, are included in the kSZ template (see Appendix C). We adopt $m_v = 2.4$ as a default, but consider other possibilities in Section 4.2.

As shown below (Section 5), for WMAP, we are mostly sensitive to nearby galaxies at a typical distance of $20h^{-1}$ Mpc. The typical apparent scale of galaxies on

the sky is thus $R_v/(20h^{-1} \text{ Mpc}) \sim m_v \times 0.63$ degrees. For $m_v = 2.4$ ($m_v = 10$ respectively), the scale is thus ~ 1.5 degrees (~ 6.3 degrees). In both cases, the modelled plasma halo is bigger than the beam size of WMAP, which is $\lesssim 0.5$ degrees.

We generate three kSZ templates, one for each bulk flow Cartesian axis, and then fit simultaneously all components. In Figure 1, we show the kSZ template obtained before multiplying by a dipolar bulk-flow and normalised to 100 km s^{-1} , in the inward direction. Equivalently, it would be the kSZ signal that would be produced if all selected galaxies were moving at the same 100 km s^{-1} , speed towards us. Using a different colour scale, this same map corresponds to the optical depth. Averaging over pre-beamed non-null pixels, the average optical depth is 1.8×10^{-4} for $m_v = 2.37$. For $m_v = 10$, this same average yields 2.6×10^{-4} , a 44% increase.

The kSZ template exhibits smaller structures than the tSZ signal. Additionally, the kSZ signal does not depend on the frequency. These two features make the kSZ signal far more difficult to detect in the CMB data than the tSZ signal. Nevertheless, we note that the kSZ signal should dominate the tSZ signal on the scale of the plasma halo of a galaxy. The ratio R_{TK} between the tSZ signal and the kSZ is given by

$$R_{\text{TK}} = \frac{\Delta T_{\text{tSZ}}}{\Delta T_{\text{kSZ}}} \simeq \frac{2k\bar{T}_e}{m_e V c} \quad (14)$$

with V the global velocity of the galaxy, \bar{T}_e the mean temperature of electrons in the halo, m_e the mass of electrons. With $\bar{T}_e = 10^6 \text{ K}$, $m_e c^2 = 511 \text{ keV}$ and

$V = 300 \text{ km s}^{-1}$, we get $R_{\text{TK}} = 0.34$. Additionally, the bulk flow gives a dipolar modulation of the galaxy distribution on the sky, whereas the tSZ signal would simply trace cluster (or galaxy) distribution. Consequently, we do not expect a systematic contamination by tSZ at the galaxy level.

3.2 tSZ model

The tSZ signal is generated by hot and dense ionised gas. These conditions are found in the intracluster medium, and clusters of galaxies have already been detected using this effect (for a review see e.g. Birkinshaw 1999). We use the model given in the appendix of Afshordi et al. (2005) for the temperature and gas density profiles in clusters. Given the X-ray luminosity, the RBC catalogue provides the virial mass M_{vir} from which we derive the virial radius $R_{\text{vir}} = (2GM_{\text{vir}}/(\Delta_{\text{vir}}H^2))^{1/3}$, with $\Delta_{\text{vir}} = 200$, G the gravitational constant and H the Hubble constant. Using this mass estimate, the model predicts the two profiles assuming hydrostatic equilibrium. The temperature change due to the presence of a cluster in direction \hat{n}_c is given by:

$$\Delta T_{\text{tSZ}}(\nu, \hat{n}) = -2T_{\text{CMB}} \sigma_T f_{\text{tSZ}} \left(\frac{h\nu}{kT_{\text{CMB}}} \right) \int_0^{\sqrt{(2R_{\text{vir}})^2 - r_c^2}} n_e \left[\sqrt{s^2 + r_c^2(\hat{n})} \right] \frac{kT_e \left[\sqrt{s^2 + r_c^2(\hat{n})} \right]}{m_e c^2} ds, \quad (15)$$

with $n_e(s)$ and $T_e(s)$, respectively denoting the density and temperature of the free intracluster electrons at a distance s from the centre of the cluster, ν the frequency at which the temperature is observed. The dependence $f_{\text{tSZ}}(x)$ on the frequency $x = h\nu/kT_{\text{CMB}}$ is

$$f_{\text{tSZ}}(x) = 4 - x \coth\left(\frac{x}{2}\right). \quad (16)$$

r_c is the projected distance from the centre of the cluster. It has the same expression as for galaxies, given in Equation (12). Note that we stop the integration at twice the virial radius of the cluster.

An example of the tSZ template in the W channel of WMAP is given in Figure 2. We have selected all 781 clusters with redshift $z \leq 0.3$, from RBC. With our normalisation the resulting signal is typically at a level of a fraction of a milli-Kelvin.

3.3 Point source model

We follow Afshordi et al. (2004) and Jarosik et al. (2011) in modelling the effective temperature of point sources in the CMB sky. We remind the reader of their main result:

$$\Delta T(\hat{p}_j) = \mathcal{N}_{\text{PS}} \Gamma_c^{\text{bb}} a(\nu_c) L_{\text{rad},c} \sum_i \frac{\phi_i}{L} \delta_S(\hat{n}_i, \hat{p}_j), \quad (17)$$

with Γ_c^{bb} is a conversion factor between physical flux and antenna temperature that depends on the channel c , \hat{p}_j is the direction of the j -th pixel, and \hat{n}_i is the direction of observation of the galaxy i . We also use $\delta_S(\hat{n}, \hat{m})$, which is one if \hat{n} and \hat{m} corresponds to the same pixel of the

CMB map, and zero otherwise. $a(\nu_c)$ accounts for the difference between antenna temperature and thermodynamic temperature (Bennett et al. 2003):

$$a(\nu) = \frac{4 \sinh^2(x/2)}{x(\nu)^2}. \quad (18)$$

$L_{\text{rad},c}$ is the average point source luminosity in the channel c . \mathcal{N}_{PS} is a normalisation factor to account both for pixelisation and the normalisation of the beam. \bar{L} is the luminosity density of galaxies in the considered catalogue. We use the typical value derived by Lavaux & Hudson (2011) for normalising: $\bar{L} \equiv 4 \times 10^8 h^{-2} L_{\odot}$. ϕ_i is the observed flux of the galaxy i :

$$\phi_i = 10^{0.4(M_{K,\odot} - m_i + 25)}, \quad (19)$$

with $M_{K,\odot}$ the intrinsic luminosity of the sun in the K band of 2MASS: $M_{K,\odot} = 3.29$. Page et al. (2003) gives the value for Γ_c^{bb} in the case of free-free emission (scale free spectrum with a slope $\alpha = -0.1$). The point source template includes only galaxies with apparent magnitude $K_{20} \leq 13.5 - A_K$ (with A_K the extinction derived from the reddening (Schlegel et al. 1998)). The relation between the reddening and the extinction is

$$A_K = 0.35 E_{(B-V)}, \quad (20)$$

where the constant of proportionality is obtained from the relation between extinction in K band and in V band (Cardelli et al. 1989).

3.4 Effective mask

Since WMAP data are contaminated by strong radio sources and foreground emission, it is necessary to mask parts of the sky that may contaminate the fitting procedure. We have used the “Extended Temperature Analysis” mask (dubbed KQ75 by the WMAP collaboration) to remove Galactic contamination.

In addition, we need to allow for the fact that, due to Galactic extinction, galaxies are not uniformly detected on the sky. To ensure the completeness of the 2MASS-XSC sample, and thus of our template, we also require that the Galactic extinction $A_K < 0.1$.

The 2M++ sample has less uniform sampling at low redshift for Galactic latitudes $|b| > 10^\circ$ because at lower latitudes only the galaxies $K < 11.5$ are properly sampled. We thus add two further conditions: $A_K < 0.1$ and $|b| > 15^\circ$ to produce the effective mask. We use a conservative latitude cut to remove also as much galactic foreground as possible from the fitting. The final mask is shown in Figure 3. The M operator in Equation (5) corresponds to multiplying a pixelated temperature data by this mask.

4 RESULTS

In this Section, we present our measurement of the kSZ signal using WMAP7 data. We present the significance and the possible shortcomings of the measurement in Section 4.1.

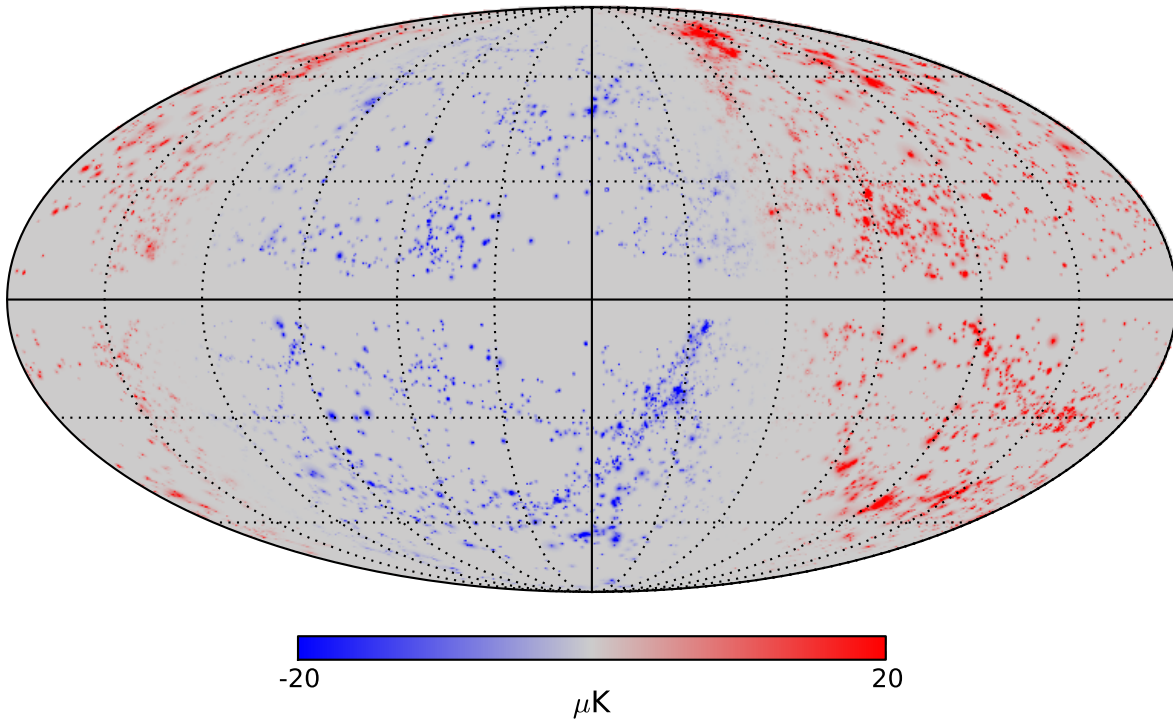


Figure 5. kSZ signal corresponding to the mean bulk-flow corresponding to the $50h^{-1}$ Mpc cut in the 2M++, limited to $|b| \geq 15^\circ$ (line 1 of Table 1).

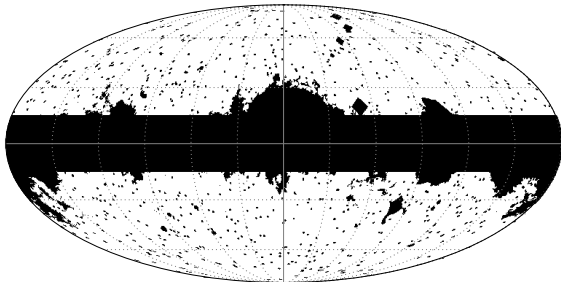


Figure 3. Mollweide projection in Galactic coordinates of one of the masks used in the analysis. This particular mask is generated from the KQ75 WMAP mask, the constraint that $A_K \leq 0.1$ and $|b| \geq 15^\circ$.

4.1 Results from 2M++

Our “default” solution is based on the templates and mask described in Section 3, with the amplitude of the templates left free. We use the best fit angular power spectrum provided by the WMAP collaboration (Komatsu et al. 2011) for a Λ CDM model obtained from WMAP7 data alone (Jarosik et al. 2011). Additionally, we independently fit the residual full sky dipole in WMAP7 maps, which could otherwise contaminate our fit of the kSZ signal, which is also dipolar, albeit localised at the positions of galaxies. We produce a set of kSZ templates with the 2M++ galaxy sample limited at different distances from the observer. All templates discard galaxies within $5h^{-1}$ Mpc which is the minimum distance at

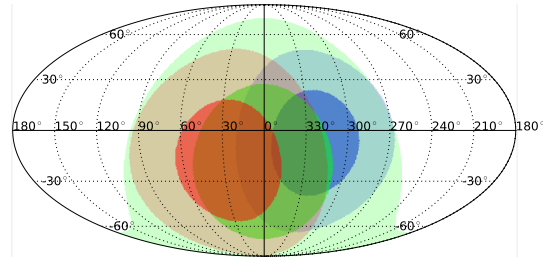


Figure 4. A Mollweide projection in Galactic coordinates of the posterior probability of the kSZ bulk-flow direction. The dark (light) areas show the direction of bulk flow at 68% (95%) probability. We have only shown the constraints corresponding to the measurement with tSZ signal masked and an isothermal density profile (line 1-3 of Table 1). The blue, green and red areas correspond to a $50h^{-1}$ Mpc, $100h^{-1}$ Mpc and $200h^{-1}$ Mpc respectively, fitting only higher galactic latitudes $|b| \geq 15^\circ$.

which redshift information can be used as an average indicator of distance. We produce subsamples limited to $50h^{-1}$ Mpc, $100h^{-1}$ Mpc, $200h^{-1}$ Mpc and fit each galaxy sample independently.

Our results are summarised in Figure 4, Table 1 and Table 2. Our results are consistent the presence of kSZ signal at the 90% level at line 1. The corresponding kSZ map is given in Figure 5.

Table 1. Kinetic Sunyaev-Zel’dovich estimates from WMAP7 maps.

Line	Sky cut ($ b \geq$)	kSZ depth (h^{-1} Mpc)	kSZ (km s^{-1})			χ^2	p_0 (%)
			V_x	V_y	V_z		
1	15°	50	559 ± 290	-412 ± 285	-93 ± 200	6.1	11
2		100	305 ± 223	7 ± 222	-119 ± 151	2.5	47
3		200	365 ± 207	183 ± 206	-141 ± 143	5.0	17

NOTE: For all the above measurements, we have used the basic mask of Section 3.4. The reported χ^2 has three degrees of freedom. There is a weak correlation between components that is accounted for in the evaluation of the χ^2 . The correlation is 14% for $V_x \times V_y$, -2% for $V_x \times V_z$ and 2.6% for $V_y \times V_z$. p_0 is the probability of the null hypothesis, namely that there is no bulk flow. An empty field means that the value is kept the same compared to the previous line. For all measurements we find consistent tSZ measurement with an amplitude of 0.72 ± 0.22 , though the bulk of the tSZ pixels are masked out. Without masking the amplitude of the tSZ is 0.85 ± 0.08 . The point source contamination signals are, in unit of 10^{-5} Jansky, 6 ± 2 (Q channel), 12 ± 7 (V channel) and 40 ± 30 (W channel).

Table 2. Robustness tests and investigation of model systematics on the kSZ signal detection.

Line	Experiment	kSZ (km s^{-1})			χ^2	p_0 (%)
		V_x	V_y	V_z		
1	tSZ masked	559 ± 290	-412 ± 285	-93 ± 200	6.1	11
2	tSZ not masked	510 ± 294	-239 ± 269	-183 ± 204	5.5	14
3	NFW, tSZ not masked	550 ± 276	-184 ± 256	-176 ± 194	5.4	15
4	tSZ not masked, $m_V = 10$	540 ± 262	-262 ± 236	-126 ± 181	6.4	10
5	tSZ not masked, σ scaling, $m_V = 2.4$	582 ± 386	-269 ± 383	178 ± 302	3.8	29
6	tSZ masked, σ scaling, limit to $M_* + 1$, $m_V = 3.59$	697 ± 460	-483 ± 442	506 ± 345	7.3	6
7	tSZ extended masking, σ scaling, limit to $M_* + 1$, $m_V = 3.59$	796 ± 478	-407 ± 451	429 ± 352	6.2	10
8	tSZ masked, $ b \geq 10^\circ$	531 ± 273	-405 ± 259	-122 ± 194	6.6	9
9	tSZ not masked, kSZ monopole	450 ± 292	-390 ± 271	-140 ± 198	5.7	13

NOTE: In all the above, we have used a mask based on the KQ75 sky cut, as indicated in Section 3.4. The notation “tSZ masked” indicates that we have masked out pixels which were expected to have un-beamed tSZ signal from the cluster sample. “tSZ extended masking” indicates that all pixels with a contamination bigger than $0.1\mu\text{K}$, after beaming in the Q channel, have been masked out. All kSZ templates have been generated from the 2M++ limited to a depth of $50h^{-1}$ Mpc.

4.2 Tests of potential systematics

In deriving our solution, we imposed the constraint that that the Galactic foreground corrections are positive. Technically, this corresponds to enforcing the constraint $\alpha_{i,\rho} > 0$, for the templates i corresponding to foregrounds. As a check on the foreground template fitting, we give in Table 3 our best fit parameters for the Galactic foregrounds (without forcing the parameter to be positive). We also show in Table 3 the value of the parameters found by the WMAP collaboration, which we have averaged by frequency channel. There is a good agreement between the two sets of parameters when we include all pixels at $|b| \geq 10^\circ$. However, there is some tension on the parameters of the $T_K - T_{K_A}$ when only pixels with $|b| \geq 30^\circ$ are included, but we note that the WMAP collaboration fitted their models after degrading their map at $N_{\text{side}} = 32$, using *all* the pixels of the maps. The cut at $|b| \geq 10^\circ$ is thus more consistent with their methodology. We conclude that our foreground fitting at full resolution is consistent with the findings of the WMAP collaboration.

After subtracting the Galactic foreground components, we are left with a signal for point-sources which is consistent with zero for the V and W channels and marginally above zero for the Q channel. The tSZ tem-

plate has an amplitude of 0.85 ± 0.08 , significant at $\sim 10.6\sigma$, and consistent with unity. A value of unity means that the physical model adopted for the tSZ effect is exactly right.

In Table 2, we investigate how different cuts or models affect the results of line 1 of Table 1. The first line of this table is a copy of the first line of Table 1. We check the impact of pixel masking in line 2. For this experiment, we use all the pixels of the map and we assume that our model for the tSZ signal is correct in average. This operation introduces a marginal change in the kSZ signal.

Our default model for the plasma halo discussed in Section 3.1 is simple and it is possible that the plasma traces halos of different mass differently, or has a different radial dependence. In lines 3 to 6, we investigate the impact of the choice of the model for the density profile of the plasma halo. Using a Navarro-Frenk-White profile (Navarro et al. 1996) instead of an isothermal profile barely changes the result (line 3 vs. line 1). We have attempted to scale up the plasma halo radius R_V by changing the multiplicative factor m_V to the extreme value $m_V = 10$. Increasing this factor may be useful for including the presence of smaller haloes and/or filamentary WHIM that are clustered with the galaxy. This operation

Table 3. Foreground contamination of the map estimated from the data.

Origin	Dust map			$T_K - T_{KA}$ map			H_α map ($\mu\text{K R}^{-1}$)		
	Q	V	W	Q	V	W	Q	V	W
$ b \geq 10^\circ$	0.4 ± 0.2	0.6 ± 0.2	1.3 ± 0.2	0.32 ± 0.02	0.12 ± 0.02	0.06 ± 0.02	1.7 ± 0.4	1.2 ± 0.4	0.8 ± 0.4
$ b \geq 30^\circ$	-0.6 ± 0.3	-0.4 ± 0.3	0.3 ± 0.3	0.42 ± 0.02	0.23 ± 0.02	0.17 ± 0.02	1.8 ± 0.4	1.1 ± 0.4	0.7 ± 0.4
WMAP7	0.20	0.47	1.28	0.23	0.047	0.00	1.22	0.78	0.43

NOTE: We show the best fit amplitude for each of the templates provided by the WMAP collaboration (Gold et al. 2011), at a resolution of $N_{\text{side}} = 512$. The first two lines has been obtained in this work, using the indicated sky cuts. The last line has been derived from table 2 of Gold et al. (2011).

does not affect mean recovered velocity and slightly reduces the error bars by introducing more pixels in the correlation. This suggests for WMAP that it is difficult to measure the radial extent of clustered electrons via the strength of the kSZ effect

It is also possible that the mapping between stellar mass traced by K -band light and plasma halo mass differs from our fiducial choice for which the mass is proportional to $L^{1/3}$. In lines 5 to 7, we have introduced the scaling of the velocity dispersions with the luminosity of the galaxy according to

$$\sigma(L) = 160 \text{ km s}^{-1} \left(\frac{L}{L_*} \right)^{1/3}, \quad (21)$$

where $L_* = 3.9 \cdot 10^{10} h^{-2} L_\odot$. This choice effectively forces mass to be proportional to the luminosity. The first impact of such a choice is just to increase error bars (line 5), which is expected as the kSZ signal from small galaxies is strongly reduced. Limiting the sample to the 4450 galaxies within $50h^{-1}$ Mpc which have an absolute magnitude brighter than $M_* + 1$ and adjusting m_V accordingly (Appendix C) leads to a strong change in the flow amplitude along the Z -direction (line 6). The cause of this change is not understood. In line 7, we have tried to remove as much tSZ signal as possible by masking out pixels which were contaminated at a level larger than $0.1 \mu\text{K}$ after beaming according to our model and the RBC cluster catalogue. The kSZ signal does not change compared to line 6.

In line 8, we have reduced the masked regions to include more temperature measurements at lower galactic latitudes. Compared to the fiducial experiment in line 1, the error bars are slightly smaller in all directions. The mean values per directions are in perfect agreement with the values in line 1.

For the case 9, we consider whether we may miss a kSZ monopole component and/or a tSZ component generated by the plasma halo around galaxies. Not accounting for this effect in our model may bias the results. To assess this effect, we add a new template that corresponds to a kSZ monopole. We find a monopole for the kSZ template equal to a mean (inward) peculiar velocity of $-243 \pm 152 \text{ km s}^{-1}$. The χ^2 value takes into account errors correlation between the component, which are introduced by the mask.

In Figure 6, we show the likelihood contours of the direction of the kSZ signal for two different mask cuts

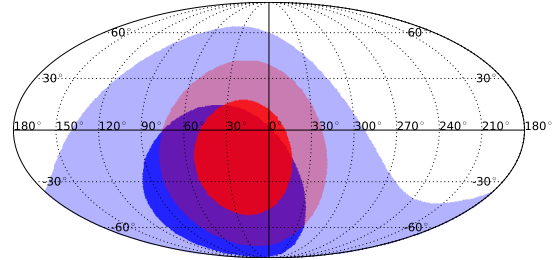


Figure 6. Test of contamination of the kSZ signal by the Galactic plane. We show the direction of the fitted kSZ bulk flow in two cases where we only use pixels with $|b| \geq 10^\circ$ ($|b| \geq 30^\circ$ respectively) for the red (blue respectively) contours. In both cases, we have limited our galaxy sample for generating the kSZ templates to $200h^{-1}$ Mpc.

$|b| \geq 10^\circ$ and $|b| \geq 30^\circ$. The test is run for a kSZ depth of $200h^{-1}$ Mpc. There is no sign of strong variation of the peak of the likelihood by cutting $\sim 40\%$ of the available pixels. The only visible impact is a widening the distribution.

Finally, in the left panel of Figure 7 we show the result of a jackknife test obtained by removing the part of the sky that corresponds to the indicated root pixel of the HEALPIX mesh. These root pixels are given in the right panel of Figure 7. This test shows that, at a given depth, the kSZ signal is stable. We note that for deeper measurements, the jackknife causes the recovered flow to scatter along the X -direction and thus could be interpreted as a sign of contamination by the WMAP “haze” (Finkbeiner 2004; Pietrobon et al. 2011). Correlations between galaxies and Milky-Way extinction properties are likely in the bulge and that could correlate the kSZ signal with the haze. We note that the effect of this haze would go in the opposite direction as what we obtain for the kSZ in all slices: it creates a positive temperature fluctuation which would push the kSZ signal towards negative X . In our case, the signal is pushed towards positive X . Additionally, the push would be affected by removal of the the galactic bulge part in the Jackknife test, which is not the case.

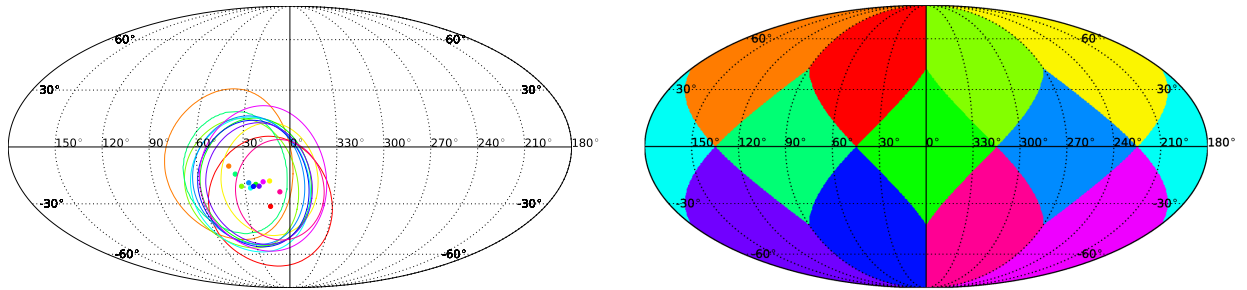


Figure 7. In the right panel, we show the change in direction of the flow resulting from a jackknife test. We removed the indicated root pixel of the HEALPIX mesh for each test. We have used a low-Galactic latitude cut of the mask with $|b| \geq 10^\circ$. The kSZ template has been generated with galaxies within a $5\text{--}200h^{-1}$ Mpc from the Local Group. The line iso-density contour gives the area corresponding to 68% of probability. The root pixels of the HEALPIX mesh are given in the right panel.

Table 4. Bulk flows at depths $> 200 h^{-1}$ Mpc from the kinetic Sunyaev-Zel’dovich effect alone.

Experiment	Typical depth (h^{-1} Mpc)	kSZ (km s^{-1})			χ_0^2	p_0 (%)	χ_{KAEEK}^2	p_{KAEEK} (%)
		V_x	V_y	V_z				
2MASS-XSC $K \leq 14$	470	160 ± 141	211 ± 124	-11 ± 112	4.3	23		
Kashlinsky et al. (2010)	175-260	174 ± 407	-849 ± 351	348 ± 342	7.1	7	9.1	2.8
	260-380	428 ± 375	-1029 ± 323	575 ± 316	14.7	0.2	16.3	9×10^{-2}
	270-530	352 ± 304	-713 ± 262	652 ± 256	15.2	0.16	16.1	1×10^{-1}

NOTE: χ_0^2 , and its associated probability p_0 , represent the probability that the flow is zero. χ_{KAEEK}^2 , and its associated probability p_{KAEEK} , is the probability that the results of Kashlinsky et al. (2010) are in agreement with our result based on 2MASS-XSC.

4.3 Results from 2MASS-XSC

Finally, we have estimated the amplitude of the bulk flow using the entire 2MASS-XSC limited to $K_{\text{fe}} \leq 14.0$ as the kSZ template. After removing nearby large galaxies and parts of the sky that could suffer strong reddening, we have 959 554 galaxies with $K_{\text{fe}} \leq 14.0$. As the 2MASS-XSC does not have redshifts, we randomly generated distances for each galaxy based on their apparent magnitude and an assumed Schechter function for the distribution of absolute magnitudes of galaxies. Specifically, we used the Schechter parameters given in Lavaux & Hudson (2011) for the 2M++: $\alpha = -0.73$, $M_* = -23.17$. The result is not strongly dependent on these parameters. We estimated the kSZ bulk flow from an ensemble of ten realisations of those distances. The scatter in bulk flow from one realisation to the other is $\sim 60 \text{ km s}^{-1}$ by component. The median depth of such a survey is $470h^{-1}$ Mpc, with a mean distance of $\sim 550h^{-1}$ Mpc because of the long tail of the distribution. The results are given in Table 4 and are consistent with no bulk flow on these very large scales, with a 95% upper limit of 520 km s^{-1} , after correction for random error biasing. The standard deviation per component of the kSZ signal is $\sim 100 \text{ km s}^{-1}$. We have not found any evidence for a bulk flow that would be inconsistent with Λ CDM. However, our results disagree

with the bulk flow found by Kashlinsky et al. (2010) at the 4.2σ level^{3 4}.

5 BULK FLOWS AND THE FRACTION OF FREE ELECTRONS

While the bulk flow on very large scales is controversial, the existence of a bulk flow at depths of $< 50 h^{-1}$ Mpc, due to local superclusters such as Virgo, the Great Attractor region and Perseus-Pisces, is not controversial: there is good agreement between peculiar velocity surveys as well as with the predictions of the density field. The kSZ signal is the product of the electron density times the velocity, i.e. the momentum. Therefore, we can take the existence of the bulk flow as a given, and instead determine the density of free electrons.

In order to do so, we must first consider the volume that is actually being sampled by combination of the kSZ template and the WMAP data. Although our template extends to $200 h^{-1}$ Mpc, nearby galaxy haloes have more

³ A similar conclusion was reached in Dai et al. (2011) through analysis of supernovae Ia at $z < 0.05$.

⁴ After initial submission of this paper, Li et al. (2012) published an attempt to detect the “Dark Flow” using a cross-correlation of SDSS galaxy positions and WMAP temperature measurements. While the authors found some evidence of a correlation, they acknowledge that they were not able to reliably link it to a large-scale bulk flow.

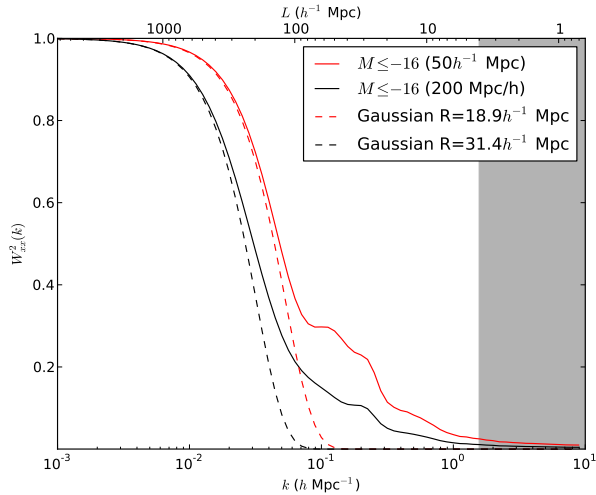


Figure 8. We show the window function $\mathcal{W}^{x,x}(k)$ (component along the X axis of the bulk flow) for our two sample selections: $50h^{-1}$ Mpc (red lines) and $200h^{-1}$ Mpc (black lines). They have been derived using Eq. (D22) of Appendix D. We show in dashed lines the fit to a Gaussian window function to the corresponding window functions. The part of the window function highlighted by the greyed area may not be trusted because of the approximations that we have used.

weight, and so the bulk flow measured is not simply volume limited. We discuss the effective volume of the kSZ measurement below before discussing the fraction of free electrons.

5.1 Kinetic Sunyaev-Zel’dovich effect window function

The amplitude and direction of the kSZ effect may be interpreted as a bulk flow obtained from the weighted average of the peculiar velocities of galaxies. The weighting depends both on the selection cut and the limitations of the instrument used to observe the CMB. The weighted average procedure may be modelled by the convolution of the peculiar velocity field by a kernel, called window function. We argue that the bulk flow estimate must have a similar window function to that used in a maximum likelihood analysis of galaxy distance surveys. We may assume, e.g., that galaxies have all the same physical size $\sim R_v$. Their sizes on the sky, in terms of number of pixels, are thus $\sim R_v^2/z^2 \propto 1/d^2$, with z their redshifts and d their angular distances. The number of pixels affected by each galaxy in the kSZ template is thus scaling as $1/d^2$. If for simplicity we assume that the pixel noise is homogeneous, the weight for the peculiar velocity of each galaxy becomes proportional to the inverse squared distance of this galaxy. This is exactly the same case for bulk flow derived from maximum likelihood estimate from galaxy distances. In that case, the peculiar velocity errors scale as the distance d , which leads to the same weight per galaxy as the kSZ effect.

We give a quantitative derivation of this window function in Appendix D where we also discuss the limitations of this calculation. Figure 8 shows the square of the window function of the bulk flow in the Galactic bulge

direction (X axis). We also show the window function corresponding to the convolution with a Gaussian kernel W_G of size R defined as

$$W_G(\mathbf{r}) = \frac{1}{(2\pi)^{3/2} R^3} e^{-\frac{r^2}{2R^2}}. \quad (22)$$

The size R is determined such that the second derivatives of the actual window function and of the Gaussian kernel are equal. The measurement, based on galaxies within $50h^{-1}$ Mpc, seems to correspond to a $18.9h^{-1}$ Mpc Gaussian window on large scales. Similarly, the measurement using galaxies within $200h^{-1}$ Mpc corresponds to a Gaussian window of $31.4h^{-1}$ Mpc. We have evaluated the window function for the Galactic Y and Z components of the bulk flow and we have obtained similar results for the probed scales. Because the masked galaxy distribution is anisotropic, the window functions are not strictly equal for the three components of the bulk flow. The important point is that the kSZ signal is dominated by galaxies on scales significantly nearer than the limiting depth.

5.2 Comparison with published bulk flows and the free electron fraction

When only galaxies within $50h^{-1}$ Mpc are used in the kSZ template, we find $|V| = 533 \pm 263 \text{ km s}^{-1}$ (after correction for “error biasing”⁵) in the direction $l = 324 \pm 27$, $b = -7 \pm 17$. This is similar in direction and amplitude to recent bulk flows based on classical distance measurements. For example, at a similar depth, the “Seven Samurai” (7S) found $V = 599 \pm 104 \text{ km s}^{-1}$ in the direction $l = 312 \pm 11$, $b = 6 \pm 10$ (Dressler et al. 1987) using the $D_n - \sigma$ distance indicator for early-type galaxies. Table 5 shows three recent bulk flow measurements derived using three different methods, along with the characteristic scale for averaging the peculiar velocities. We have selected these three bulk flows because they probe similar volumes to that probed by the kSZ measurement of Line 1 of Table 1. For example, the “SHALLOW” sample analysed by Watkins et al. (2009) includes measurements from surface brightness fluctuations (Tonry et al. 2001) and the ENEAR sample (Bernardi et al. 2002), an updated version of the 7S sample quoted above, whereas the SFI++ sample contains the latest Tully-Fisher distances. The result from Lavaux et al. (2010) is instead a predicted bulk flow, assuming that 2MASS-selected galaxies trace the mass. Figure 9 shows the direction of the bulk flow for kSZ measurement (limited to $50h^{-1}$ Mpc) and for the data sets discussed above. The directions are in good agreement.

Given the agreement in direction, we may assume that the amplitude itself is significant. The amplitude of the kSZ signal, expressed as bulk flow components $\mathbf{V}_{\text{bulk,kSZ}}$, may be modelled as the following:

$$\mathbf{V}_{\text{bulk,kSZ}} = \tilde{f} \mathbf{V}_{\text{bulk}}, \quad (23)$$

⁵ The velocity amplitude is a positive number so random errors will bias the true amplitude upward. We correct for this by subtracting off in quadrature the uncertainties in each Cartesian component of the flow.

Table 5. Summary of bulk flows from in the literature with similar depths as the kSZ measurement.

Reference	Scale (h^{-1} Mpc)	Filter	V_x (km s^{-1})	V_y (km s^{-1})	V_z (km s^{-1})	$ V $ (km s^{-1})	l ($^\circ$)	b ($^\circ$)
Watkins et al. (2009)	20	Gaussian	85 ± 27	-228 ± 43	53 ± 26	253 ± 40	291 ± 7	12 ± 6
	SHALLOW	MLE	190 ± 33	-259 ± 29	110 ± 23	342 ± 30	306 ± 6	19 ± 4
	SFI++	MLE	117 ± 28	-331 ± 28	96 ± 20	365 ± 27	290 ± 5	15 ± 3
Lavaux et al. (2010)	50	Top-hat	227 ± 77	-270 ± 78	136 ± 78	393 ± 75	310 ± 13	20 ± 11

Note: In the case of “SHALLOW” and “SFI++”, we have used the Maximum Likelihood Estimator (MLE) values quoted in Watkins et al. (2009). The value given reported as $20h^{-1}$ Mpc Gaussian is obtained using the minimum variance estimator applied on the “COMPOSITE” sample.

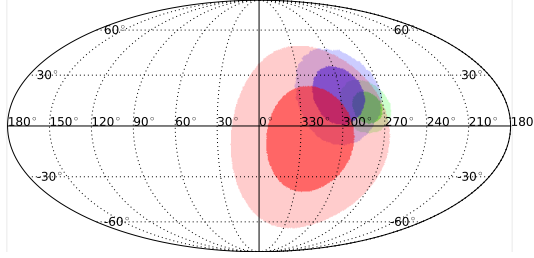


Figure 9. We have drawn the 68% and 95% probability limit for the kSZ signal direction and some of the bulk flows given in Table 5. Green: Watkins et al. (2009), limited to $20h^{-1}$ Mpc Gaussian. Blue: Lavaux et al. (2010), limited to $50h^{-1}$ Mpc Top-hat. Red: kSZ signal, template generated with galaxies $cz \leq 5000 \text{ km s}^{-1}$.

with $\tilde{f} = f_e(\sigma/160 \text{ km s}^{-1})^2$, f_e being the fraction of free electrons and σ modelling the unknown normalisation of the density profile of the galactic plasma halo. \tilde{f} is taken as a free parameter for this subsection, \mathbf{V}_{bulk} the bulk flow components as determined by other methods listed in Table 5. We may derive the posterior probability of \tilde{f} using Bayes identity, which, up to a normalisation, is:

$$P(\tilde{f}|\mathbf{V}_{\text{bulk,kSZ}}, \mathbf{V}_{\text{bulk}}) \propto \int d^3\mathbf{V}_{\text{bulk,true}} P(\mathbf{V}_{\text{bulk,kSZ}}|\tilde{f}, \mathbf{V}_{\text{bulk,true}}) P(\mathbf{V}_{\text{bulk,true}}), \quad (24)$$

with

$$P(\mathbf{V}_{\text{bulk,kSZ}}|\tilde{f}, \mathbf{V}_{\text{bulk}}) = \mathcal{G}(\tilde{f}\mathbf{V}_{\text{bulk,true}}, \sigma_{\text{kSZ}}), \quad (25)$$

and

$$P(\mathbf{V}_{\text{bulk,true}}) = \mathcal{G}(\mathbf{V}_{\text{bulk}}, \sigma_{\text{bulk}}). \quad (26)$$

In the above expressions, we have used the notation $\mathcal{G}(\mathbf{m}, \mathbf{s})$ for a three dimensional Gaussian probability, with the mean m_i and the standard deviation s_i for the same component. σ_{kSZ} (σ_{bulk} respectively) is given by the errors on the components quoted in Table 1 (Table 5 respectively). Effectively the posterior probability (24) may be written as a likelihood function

$$\mathcal{L}(\tilde{f}) = \sum_{i=1}^3 \left[\left(\frac{V_{i,\text{bulk,kSZ}} - \tilde{f}V_{i,\text{bulk}}}{\tilde{f}^2\sigma_{i,\text{bulk}}^2 + \sigma_{i,\text{kSZ}}^2} \right)^2 + \log \left(\tilde{f}^2\sigma_{i,\text{bulk}}^2 + \sigma_{i,\text{kSZ}}^2 \right) \right]. \quad (27)$$

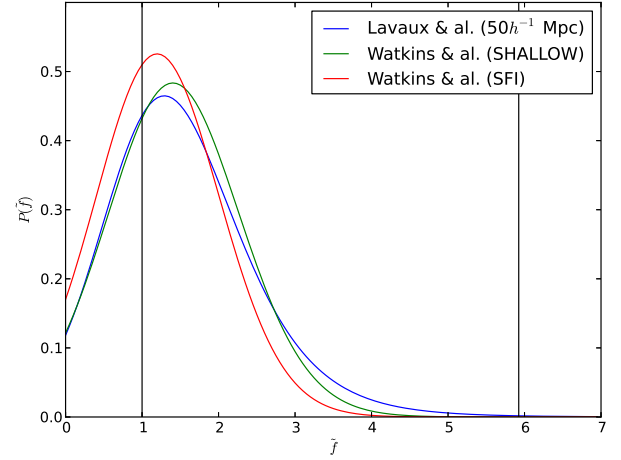


Figure 10. The posterior distribution for the \tilde{f} factor assuming different measured bulk flows for a single kSZ measurement given by line 1. The left (right respectively) black solid vertical line correspond to $\tilde{f} = 1$ ($\tilde{f} = \Omega_m/\Omega_b = 5.92$ respectively).

We show the posterior distribution of the parameter \tilde{f} in Figure 10 for different choices of the published bulk flows against one single of our kSZ measurement. We are taking the line 1 of Table 1 as the fiducial kSZ measurement. Assuming the bulk flow for the SHALLOW sample in Watkins et al. (2009), the posterior peaks at $\tilde{f} = 1.4^{+1.02}_{-0.99}$ (68% confidence limit). For the bulk flow of the SFI sample, this value becomes $\tilde{f} = 1.2^{+0.95}_{-0.94}$. Assuming Lavaux et al. (2010) cut at $50h^{-1}$ Mpc top-hat, the posterior peaks at $\tilde{f} = 1.29^{+1.1}_{-0.92}$. For information, we have shown two extreme choices of choosing the amount of baryons in galaxies. The choice $\tilde{f} = 1$ corresponds to considering that galaxies have a dark matter halo and all baryons are ionised in the plasma halo. For indicative purposes, we have shown $\tilde{f} = \Omega_{\text{m,fid}}/\Omega_b = 5.92$ in Figure 10, $\Omega_{\text{m,fid}} = 0.258$. We would measure such a value if the density of baryons were equal to the mean density of dark matter. We note that all posteriors are in agreement with a choice of $\tilde{f} = 1$. The ratio of the posterior at its maximum to its value for $\tilde{f} = 0$ in the best case (green curve, SHALLOW sample) is 3.97. For the blue and red curve, this ratio is 3.93 and 3.08 respectively. According to Jeffreys (1961), a ratio of 3.97 corresponds to *substantial evidence* against the null hypothesis there are no free electrons in galaxy halos.

6 DISCUSSION AND FUTURE WORK

There are several ways in which this measurement can be improved in the near future. First, improved CMB data is anticipated from SPT (Schaffer et al. 2011) and from the PLANCK mission. We discuss below the improvement in signal-to-noise expected from PLANCK. Moreover, we anticipate a more detailed treatment of the peculiar velocity field, an improved understanding of the halo model and of the distribution of free electrons around galaxies.

6.1 Forecast for PLANCK

In this section, we estimate the noise covariance matrix of the three components of the bulk flows for the maps obtained from the PLANCK probe. The inverse covariance matrix is given by Equation (7). Neglecting the impact of the other foreground components, assuming the noise is homogeneous on the sky and no masking, the covariance matrix C_B of the kSZ bulk flow becomes diagonal in spherical harmonic space and simplifies to:

$$C_{B,i,j}^{-1} = t_i^\dagger \left(\sum_{c,c'} B_c C_{c,c'}^{-1} B_{c'}' \right) t_j = \sum_{\ell} (2\ell + 1) T_{i,j,\ell} \sum_{c,c'} B_c \left(\delta_{c,c'} N_{c,\ell}^{-1} - \frac{B_{c,\ell} B_{c',\ell} C_{\ell} N_{c,\ell}^{-1} N_{c',\ell}^{-1}}{1 + C_{\ell} \sum_c N_{c,\ell}^{-1} B_{c,\ell}^2} \right) B_{c'}, \quad (28)$$

with $T_{\ell,i,j}$ the angular cross power spectrum of the kSZ template between the component i and j of the bulk flow. For a single channel, this reduces to:

$$C_{B,i,i}^{-1} = \sum_{\ell} (2\ell + 1) \frac{T_{i,i,\ell} B_{\ell}^2}{N_{\ell} + C_{\ell} B_{\ell}^2}. \quad (29)$$

We give the forecast estimate for the channel W of WMAP7 in Table 6. In this same table, we also report the actual errors that we obtained using the full method. To make a forecast for the sensitivity that we expect using PLANCK maps, we consider the map at a frequency of 100 GHz. According to The Planck Collaboration (2006), the noise at resolution of $N_{\text{side}} = 1024$ is $\sim 7 \mu\text{K}$ for the temperature. The beam is modelled using a Gaussian with a Full-Width-Half-Maximum equal to 10 arcmins. The last column of the Table 6 gives the standard deviation expected for the velocity components of the bulk flow with these parameters. We have also tried our forecast with a more complex model based on the published Planck noise properties (Zacchei et al. 2011), which increases the errors reported in Table 6 by $\sim 20\%$. Also note that these are the errors for the $50h^{-1}$ Mpc cut. PLANCK is able to reach much more distant galaxies.

There is a good agreement between the estimated value of the noise for WMAP data and the actual noise amplitude that we measure using the complete analysis of Section 2. This gives us some confidence that the projection for PLANCK is realistic. We note that, mainly due to the reduction of the beam width, the noise should go down by a factor of two to three by using PLANCK data compared to WMAP data. This estimate does not take

Component	WMAP7 obtained (km s ⁻¹)	WMAP7 forecast (km s ⁻¹)	PLANCK forecast (km s ⁻¹)
x	290	305	120
y	285	277	111
z	200	224	93

Table 6. Standard deviation estimates on bulk flow components for the kSZ templates generated from the 2M++ catalogue cut at a depth $50h^{-1}$ Mpc.

into account possible additional foreground contamination. If the bulk flows stay at the same amplitude as we have estimated from WMAP data, that could give us a $\sim 5.4\sigma$ detection of the kSZ effect. If the bulk flow is at the level of that found for the SFI++ sample (Watkins et al. 2009), the significance could decrease to 2.2σ . It must be nonetheless noted that we have neglected all contributions from the multi-channel analysis in this prediction. The high-frequency channels would clearly help to remove the contribution of the tSZ signal. Additionally, the temperature data from the PLANCK mission have sufficient angular resolution to probe deeper flows on scales up to $200h^{-1}$ Mpc scale with better sensitivity. As a final note, we assume that the kSZ signal has the same amplitude as what is expected from the bulk flow given by the SHALLOW sample in Table 5. In this case, we forecast that the constraints on the baryon density in plasma haloes of galaxies from the PLANCK mission should be $\Delta\bar{f} \sim 0.2$, instead of ~ 0.9 as obtained in Section 5.2.

6.2 Model improvements

There are several ways in which the model for the free electron momentum field will be improved.

(i) The model for the flow field will be updated. In this paper, for simplicity, we have modelled the peculiar velocity field as a simple bulk flow, a low order moment of the peculiar velocity field. However, as suggested by Ho et al. (2009) and Shao et al. (2011), by using linear perturbation theory and an assumption about the relationship between mass and light in haloes (linear biasing or the halo model), we can predict the peculiar velocities of individual galaxies (Yahil et al. 1980; Strauss et al. 1992; Hudson 1994) to an accuracy of $\sim 150 \text{ km s}^{-1}$ (Willick & Strauss 1998) or better using a non-linear reconstruction (Lavaux et al. 2008, 2010). These predictions scale with the parameter $\beta = f(\Omega_m)/b$ where $f \sim \Omega_m^{0.55}$ for ΛCDM and b is a bias factor, and so the kSZ effect will allow us to get an independent measurement of this parameter.

(ii) We are using galaxies as a tracer of the distribution of free electrons, but we can improve this model in several ways. First, the scaling of halo mass and radius with galaxy luminosity or stellar mass can be updated using results from abundance matching (Marinoni & Hudson 2002; Yang et al. 2003; Guo et al. 2010) or weak lensing studies of low redshift galaxies (Mandelbaum et al. 2006; van Uitert et al. 2012). Second, high-resolution hydrodynamical cosmological simulations can be used to get

a better handle on the link between galaxy halo profiles and their cross-correlations with the distribution of free electrons (as in e.g. Shao et al. 2011; Peirani et al. 2012).

7 CONCLUSION

We have developed and applied a method for estimating bulk flows from kSZ signals in temperature maps of the Cosmic Microwave Background. This method is based on a likelihood analysis of the amplitude of a set of template maps derived from catalogues of galaxies. Assuming an isothermal model for the galaxy plasma halo, we have derived template maps for the kinetic Sunyaev-Zel'dovich from the 2M++ galaxy catalogue. The thermal Sunyaev-Zel'dovich signal is derived in a similar fashion from the RBC galaxy cluster catalogue, assuming the model described in Afshordi et al. (2005) for the density and temperature of the gas. To estimate the extent of the contamination by point sources residing in galaxies, we have also generated a set of templates from the 2MASS-XSC. We have fitted, independently in each channel, the standard WMAP7 foreground templates, the monopole and the dipole.

The amplitude of the tSZ signal is measured with a high accuracy at 13σ confidence. We have found evidence at the 90% confidence level for the presence of a kSZ signal in WMAP7 data. We have not detected any significant contamination by point sources. All the results are presented after having marginalised over the Galactic foreground emissions.

Interpreting the kSZ signal as the signature of a bulk flow, we derive an amplitude, when only galaxies within $50h^{-1}$ Mpc are included in the template, of $|V| = 533 \pm 263$ km s $^{-1}$, in the direction $l = 324 \pm 27$, $b = -7 \pm 17$, in excellent agreement with the "Seven Samurai" bulk flow (Dressler et al. 1987) and other recent determinations on similar scales. If we extend selection up to $200h^{-1}$ Mpc, we find $|V| = 284 \pm 187$ km s $^{-1}$, in the direction $l = 26 \pm 35$, $b = -17 \pm 19$. The kSZ bulk flow at $50h^{-1}$ Mpc is statistically in agreement with other measurements obtained from either galaxy peculiar velocities, observed or modelled. This comparison can be translated into a measurement of the fraction of baryon in galaxies. We found substantial evidence of baryons in the galaxy plasma halo, compatible with the mean density of baryons derived from WMAP7 (Komatsu et al. 2011). PLANCK data should be able to reduce the statistical error bars on the kSZ measurement by a factor two to three. If the signal stays at the present value, the evidence may be increased to 5.4σ , excluding improvements due to the high frequency channels for removing tSZ contamination. Realistically, if the bulk flow is as given by Watkins et al. (2009), then the evidence would be at the 2.2σ level.

ACKNOWLEDGEMENTS

NA and MJH acknowledge the preliminary work of Matthias Müller on a similar project.

This publication makes use of data products from

the Two Micron All Sky Survey, which is a joint project of the University of Massachusetts and the Infrared Processing and Analysis Center/California Institute of Technology, funded by the National Aeronautics and Space Administration and the National Science Foundation.

GL acknowledges support from CITA National Fellowship and financial support from the Government of Canada Post-Doctoral Research Fellowship and NSF Grant AST 07-08849, AST 09-08693. MH acknowledges support from NSERC.

Research at Perimeter Institute is supported by the Government of Canada through Industry Canada and by the Province of Ontario through the Ministry of Research and Innovation.

This work was made possible by the facilities of the Shared Hierarchical Academic Research Computing Network (SHARCNET: <http://www.sharcnet.ca>) and Compute/Calcul Canada.

We acknowledge the use of the Legacy Archive for Microwave Background Data Analysis (LAMBDA). Support for LAMBDA is provided by the NASA Office of Space Science.

Some of the results in this paper have been derived using the HEALPix⁶ (Górski et al. 2005) package.

REFERENCES

- Afshordi N., Lin Y.-T., Sanderson A. J. R., 2005, *ApJ*, 629, 1, arXiv:astro-ph/0408560
- Afshordi N., Loh Y.-S., Strauss M. A., 2004, *Phys. Rev. D*, 69, 083524, arXiv:astro-ph/0308260
- Atrio-Barandela F., Kashlinsky A., Ebeling H., Kocevski D., Edge A., 2010, *ApJ*, 719, 77, arXiv:1001.1261
- Bennett C. L., Halpern M., Hinshaw G., Jarosik N., et al. 2003, *ApJS*, 148, 1, arXiv:astro-ph/0302207
- Bernardi M., Alonso M. V., da Costa L. N., Willmer C. N. A., Wegner G., Pellegrini P. S., Rit   C., Maia M. A. G., 2002, *AJ*, 123, 2159
- Birkinshaw M., 1999, *Physics Reports*, 310, 97, arXiv:astro-ph/9808050
- Cardelli J. A., Clayton G. C., Mathis J. S., 1989, *ApJ*, 345, 245
- Colin J., Mohayaee R., Sarkar S., Shafieloo A., 2011, *MNRAS*, 414, 264, arXiv:1011.6292
- Dai D.-C., Kinney W. H., Stojkovic D., 2011, *JCAP*, 4, 15, arXiv:1102.0800
- Dav   R., Cen R., Ostriker J. P., Bryan G. L., et al. 2001, *ApJ*, 552, 473, arXiv:astro-ph/0007217
- Dressler A., Lynden-Bell D., Burstein D., Davies R. L., Faber S. M., Terlevich R., Wegner G., 1987, *ApJ*, 313, 42
- Feldman H. A., Watkins R., Hudson M. J., 2010, *MNRAS*, 407, 2328, arXiv:0911.5516
- Finkbeiner D. P., 2004, *ApJ*, 614, 186, arXiv:astro-ph/0311547
- Fukugita M., Peebles P. J. E., 2006, *ApJ*, 639, 590, arXiv:astro-ph/0508040

⁶ <http://healpix.jpl.nasa.gov>

- Gold B., Odegard N., Weiland J. L., Hill R. S., et al. 2011, *ApJS*, 192, 15, arXiv:1001.4555
- Gorski K. M., Banday A. J., Bennett C. L., Hinshaw G., Kogut A., Smoot G. F., Wright E. L., 1996, *ApJL*, 464, L11, arXiv:astro-ph/9601063
- Górski K. M., Hivon E., Banday A. J., Wandelt B. D., Hansen F. K., Reinecke M., Bartelmann M., 2005, *ApJ*, 622, 759, arXiv:astro-ph/0409513
- Guo Q., White S., Li C., Boylan-Kolchin M., 2010, *MNRAS*, 404, 1111, arXiv:0909.4305
- Haehnelt M. G., Tegmark M., 1996, *MNRAS*, 279, 545, arXiv:astro-ph/9507077
- Hand N., Addison G. E., Aubourg E., Battaglia N., et al. 2012, *ArXiv e-prints*, arXiv:1203.4219
- Ho S., Dedeo S., Spergel D., 2009, *ArXiv e-prints*, arXiv:0903.2845
- Hudson M. J., 1994, *MNRAS*, 266, 475
- Jaffe T. R., Banday A. J., Eriksen H. K., Górski K. M., Hansen F. K., 2006, *ApJ*, 643, 616, arXiv:astro-ph/0603844
- Jarosik N., Bennett C. L., Dunkley J., Gold B., et al. 2011, *ApJS*, 192, 14, arXiv:1001.4744
- Jeffreys H., 1961, *Theory of Probability*, third edn. Oxford University Press
- Kashlinsky A., Atrio-Barandela F., 2000, *ApJL*, 536, L67, arXiv:astro-ph/0005197
- Kashlinsky A., Atrio-Barandela F., Ebeling H., 2011, *ApJ*, 732, 1, arXiv:1012.3214
- Kashlinsky A., Atrio-Barandela F., Ebeling H., 2012, *ArXiv e-prints*, arXiv:1202.0717
- Kashlinsky A., Atrio-Barandela F., Ebeling H., Edge A., Kocevski D., 2010, *ApJL*, 712, L81, arXiv:0910.4958
- Kashlinsky A., Atrio-Barandela F., Kocevski D., Ebeling H., 2008, *ApJL*, 686, L49, arXiv:0809.3734
- Keisler R., 2009, *ApJL*, 707, L42, arXiv:0910.4233
- Kocevski D. D., Ebeling H., 2006, *ApJ*, 645, 1043, arXiv:astro-ph/0510106
- Komatsu E., Smith K. M., Dunkley J., Bennett C. L., et al. 2011, *ApJS*, 192, 18, arXiv:1001.4538
- Lavaux G., Hudson M. J., 2011, *MNRAS*, 416, 2840, arXiv:1105.6107
- Lavaux G., Mohayaee R., Colombi S., Tully R. B., Bernardeau F., Silk J., 2008, *MNRAS*, 383, 1292, arXiv:0707.3483
- Lavaux G., Tully R. B., Mohayaee R., Colombi S., 2010, *ApJ*, 709, 483, arXiv:0810.3658
- Li Z., Zhang P., Chen X., 2012, *ApJ*, 758, 130, arXiv:1209.0520
- Mandelbaum R., Seljak U., Kauffmann G., Hirata C. M., Brinkmann J., 2006, *MNRAS*, 368, 715, arXiv:astro-ph/0511164
- Marinoni C., Hudson M. J., 2002, *ApJ*, 569, 101
- Masters K. L., Springob C. M., Haynes M. P., Giovanelli R., 2006, *ApJ*, 653, 861, arXiv:astro-ph/0609249
- Mody K., Hajian A., 2012, *ArXiv e-prints*, arXiv:1202.1339
- Navarro J. F., Frenk C. S., White S. D. M., 1996, *ApJ*, 462, 563, arXiv:astro-ph/9508025
- Nusser A., Davis M., 2011, *ApJ*, 736, 93, arXiv:1101.1650
- Osborne S. J., Mak D. S. Y., Church S. E., Pierpaoli E., 2011, *ApJ*, 737, 98, arXiv:1011.2781
- Page L., Barnes C., Hinshaw G., Spergel D. N., et al. 2003, *ApJS*, 148, 39, arXiv:astro-ph/0302214
- Peirani S., Jung I., Silk J., Pichon C., 2012, *ArXiv e-prints*, arXiv:1205.4694
- Pietrobon D., Gorski K. M., Bartlett J., Banday A. J., et al. 2011, *ArXiv e-prints*, arXiv:1110.5418
- Rasmussen J., Sommer-Larsen J., Pedersen K., Toft S., Benson A., Bower R. G., Grove L. F., 2009, *ApJ*, 697, 79, arXiv:0903.0665
- Rees M. J., Ostriker J. P., 1977, *MNRAS*, 179, 541
- Schaffer K. K., Crawford T. M., Aird K. A., Benson B. A., et al. 2011, *ApJ*, 743, 90, arXiv:1111.7245
- Schlegel D. J., Finkbeiner D. P., Davis M., 1998, *ApJ*, 500, 525, arXiv:astro-ph/9710327
- Shao J., Zhang P., Lin W., Jing Y., Pan J., 2011, *MNRAS*, 413, 628, arXiv:1004.1301
- Shull J. M., Smith B. D., Danforth C. W., 2011, *ArXiv e-prints*, arXiv:1112.2706
- Silk J., 1977, *ApJ*, 211, 638
- Skrutskie M. F., Cutri R. M., Stiening R., Weinberg M. D., et al. 2006, *AJ*, 131, 1163
- Soltan A. M., 2006, *A&A*, 460, 59, arXiv:astro-ph/0604465
- Strauss M. A., Davis M., Yahil A., Huchra J. P., 1992, *ApJ*, 385, 421
- Sunyaev R. A., Zeldovich I. B., 1980, *MNRAS*, 190, 413
- The Planck Collaboration 2006, *ArXiv Astrophysics e-prints*, arXiv:astro-ph/0604069
- Tonry J. L., Dressler A., Blakeslee J. P., Ajhar E. A., Fletcher A. B., Luppino G. A., Metzger M. R., Moore C. B., 2001, *ApJ*, 546, 681, arXiv:astro-ph/0011223
- Turnbull S. J., Hudson M. J., Feldman H. A., Hicken M., Kirshner R. P., Watkins R., 2012, *MNRAS*, 420, 447, arXiv:1111.0631
- van Uitert E., Hoekstra H., Franx M., Gilbank D. G., Gladders M. D., Yee H. K. C., 2012, *ArXiv e-prints*, arXiv:1211.0543
- Wandelt B. D., Larson D. L., Lakshminarayanan A., 2004, *Phys. Rev. D*, 70, 083511, arXiv:astro-ph/0310080
- Watkins R., Feldman H. A., Hudson M. J., 2009, *MNRAS*, 392, 743, arXiv:0809.4041
- White S. D. M., Rees M. J., 1978, *MNRAS*, 183, 341
- Willick J. A., Strauss M. A., 1998, *ApJ*, 507, 64
- Yahil A., Sandage A., Tammann G. A., 1980, *ApJ*, 242, 448
- Yang X., Mo H. J., van den Bosch F. C., 2003, *MNRAS*, 339, 1057, arXiv:astro-ph/0207019
- Zacchei A., Maino D., Baccigalupi C., Bersanelli M., et al. 2011, *A&A*, 536, A5, arXiv:1101.2040
- Zhang P., 2010, *MNRAS*, 407, L36, arXiv:1004.0990

APPENDIX A: DERIVATION OF THE LIKELIHOOD FROM THE MODEL

In this Appendix, we derive the Equation (2) directly from the model assumptions. We start by expressing that the primary CMB fluctuations and the instrumental noise by channel are Gaussian. They have known covariance matrices S , for the primary fluctuations, and N_c , for the channel c of the instrument. N_c may include masking effect. \tilde{N}_c , as defined in Equation (5) or N_c may both be used in the following. The likelihood of the templates, assuming the amplitudes $\alpha_{i,\rho}$ and the modes s of the primary fluctuations and given the input data, is thus:

$$\chi^2(\mathbf{s}, \{\alpha_{i,\rho}\} | \{\mathbf{d}_c\}) = \mathbf{s}^\dagger \mathbf{S}^{-1} \mathbf{s} + \sum_c \mathbf{r}_c^\dagger(\mathbf{s}, \mathbf{d}_c, \{\alpha_{i,\rho}\}) \mathbf{N}_c^{-1} \mathbf{r}_c(\mathbf{s}, \mathbf{d}_c, \{\alpha_{i,\rho}\}), \quad (\text{A1})$$

with

$$\mathbf{r}_c = \mathbf{d}_c - \mathbf{B}_c \left(\mathbf{s} + \sum_i \alpha_{i,\sigma_i(c)} \mathbf{t}_{i,c} \right), \quad (\text{A2})$$

the residual. The above terms can be reordered such that s appears only in one quadratic term:

$$\chi^2(\mathbf{s}, \{\alpha_{i,\rho}\} | \{\mathbf{d}_c\}) = (\mathbf{s} - \mathbf{s}_0)^\dagger \mathbf{S}^{-1/2} \mathbf{D} \mathbf{S}^{-1/2} (\mathbf{s} - \mathbf{s}_0) - \mathbf{s}_0^\dagger \mathbf{S}^{1/2} \mathbf{D}^{-1} \mathbf{S}^{1/2} \mathbf{s}_0 + \sum_c \mathbf{d}_c^\dagger \mathbf{N}_c^{-1} \mathbf{d}_c, \quad (\text{A3})$$

with

$$\mathbf{s}_0 = \sum_c \mathbf{S}^{1/2} \mathbf{D}^{-1} \mathbf{N}_c^{-1} \mathbf{B}_c \left(\mathbf{d}_c - \sum_i \alpha_{i,\sigma_i(c)} \mathbf{t}_{i,c} \right), \quad (\text{A4})$$

and \mathbf{D} as defined in Equation (4). The likelihood is now split into two parts:

$$\chi^2(\mathbf{s}, \{\alpha_{i,\rho}\} | \{\mathbf{d}_c\}) = (\mathbf{s} - \mathbf{s}_0)^\dagger \mathbf{S}^{-1/2} \mathbf{D} \mathbf{S}^{-1/2} (\mathbf{s} - \mathbf{s}_0) + \sum_{c,c'} \left(\mathbf{d}_c - \sum_i \alpha_{i,\sigma_i(c)} \mathbf{t}_{i,c} \right) \mathbf{C}_{c,c'}^{-1} \left(\mathbf{d}_{c'} - \sum_j \alpha_{j,\sigma_j(c')} \mathbf{t}_{j,c'} \right). \quad (\text{A5})$$

The marginalisation according to primary CMB fluctuations consists in dropping the first part, which is the only one depending on s . Equation (2) immediately follows.

APPENDIX B: ACCELERATING THE PRECOMPUTATION OF THE LIKELIHOOD

For each template $\mathbf{t}_{k,c}$ of the signal k in the frequency channel c , we define a weighted template

$$\tilde{\mathbf{t}}_{k,c} = \mathbf{S}^{1/2} \mathbf{D}^{-1} \mathbf{S}^{1/2} \mathbf{B}_{c'} \tilde{\mathbf{N}}_c^{-1} \mathbf{t}_{k,c}. \quad (\text{B1})$$

The Equations (6) and (7) may be rewritten in terms of uniquely these weighted templates. We expand the Equation (3) in the Equations (6) and (7). After some algebra, we find the expression, numerically simpler, of the covariance matrix

$$\mathbf{A}_{(i,\rho),(j,\nu)} = \sum_{\substack{c,c' \\ \sigma_i(c)=\rho, \sigma_j(c')=\nu}} \left(\mathbf{t}_{i,c}^\dagger \mathbf{B}_c \tilde{\mathbf{N}}_c^{-1} \mathbf{B}_{c'}' \mathbf{t}_{j,c'} - \mathbf{t}_{i,c}^\dagger \mathbf{B}_c \tilde{\mathbf{t}}_{j,c'} \right), \quad (\text{B2})$$

and for the maximum likelihood estimate

$$\alpha = \sum_{j,\nu} \mathbf{A}_{(i,\rho),(j,\nu)}^{-1} \left(\sum_{\substack{c \\ \sigma_j(c)=\nu}} \sum_{c'} \tilde{\mathbf{t}}_{j,c}^\dagger \mathbf{d}_{c'} \right). \quad (\text{B3})$$

Only matrices that are diagonal either in pixel space or in harmonic space are involved in the two above equations. We reduce the computational time complexity from $\mathcal{O}(N_t^2 \times N_c^2)$ to $\mathcal{O}(N_t \times N_c)$ in terms of the inversion $\mathbf{C}_{c,c'}^{-1}$.

APPENDIX C: NORMALISATION OF THE GALAXY DENSITY PROFILES

The mass of a galaxy, for which the profile is limited to the radius $R = m_V R_V$, R_V being the virial radius defined in Fukugita & Peebles (2006), is:

$$M(m_V) = \frac{2\sigma^3}{\sqrt{50}GH_0} m_V \quad (\text{C1})$$

Assuming an homogeneous distribution of galaxies, with a number of density n_* , and that the total amount of dark matter is traced by galaxies, the density of dark matter is

$$\rho_{m,g} = M(m_V) n_* = \frac{2n_*\sigma^3}{\sqrt{50}GH_0} m_V. \quad (\text{C2})$$

Comparing this quantity to the measured mean matter density,

$$\rho_m = \frac{3H_0^2}{8\pi G}\Omega_m, \quad (\text{C3})$$

gives

$$\frac{\rho_{m,g}}{\rho_m} = (0.41 \pm 0.04) m_V, \quad (\text{C4})$$

with $n_* = (1.13 \pm 0.02) 10^{-2} h^3 \text{ Mpc}^{-3}$ (Lavaux & Hudson 2011), $\Omega_m = 0.266 \pm 0.028$ (WMAP7 alone) and $\sigma = 160 \text{ km s}^{-1}$ (Fukugita & Peebles 2006). The error bar were added in quadrature to obtain the error on the fraction. This result motivates the choice of the effective radius for the matter halo around galaxies. Taking $m_V = 2.4$ yields to an agreement between the matter density estimated using galaxies and the one obtained from cosmological probes.

We have tried to use a Navarro-Frenk-White white profile instead of the isothermal profile. To normalise it in the same way, we have enforced that the mass within a virial radius of the isothermal profile is the same as for the isothermal profile.

APPENDIX D: STATISTICS OF THE KSZ ESTIMATOR OF THE BULK FLOW

For the purpose of understanding the scales probed by the estimator of Equation (6) in the case of the kSZ effect, we model the full observed temperature fluctuations due to the kSZ signal like:

$$d_{\text{obs}}(\hat{n}) = A_{\text{kSZ}} \int_0^\infty dr n_e^r(r\hat{n}) \mathbf{v}(r\hat{n}) \cdot \hat{n}, \quad (\text{D1})$$

with $v^a(\mathbf{r})$ the a component of the velocity field taken at position \mathbf{r} , A_{kSZ} the normalisation of the kinetic Sunyaev-Zel'dovich, $n_e^r(\mathbf{r})$ the density of electrons at position \mathbf{r} and \hat{n} the direction we are looking in the sky. In this work, we extract the bulk flow component by fitting a modulated dipole on the projected electron distribution. Thus the model is:

$$d_m(\mathbf{V}, \hat{n}) = A_{\text{kSZ}} \int_0^{R_s} dr n_e^m(r\hat{n}) \mathbf{V} \cdot \hat{n}, \quad (\text{D2})$$

with R_s the limiting size of the survey used to fit the velocity dipole, and $n_e^m(\mathbf{r})$ is the modelled density of electrons.

We may write the fitting procedure in spherical harmonic space. In this space, it is possible to marginalise analytically according to CMB fluctuation and to take into account beaming effects. The χ^2 corresponding to the likelihood to maximise may be written as:

$$\chi^2(\mathbf{V}) = \sum_{\ell,m} \frac{1}{C_\ell} \left| a_{\ell m}^{\text{obs}} - a_{\ell,m}^m(\mathbf{V}) \right|^2, \quad (\text{D3})$$

with $C_\ell = C_\ell^{\text{CMB}} + B_\ell^{-2} N_\ell$, N_ℓ being the noise power spectrum of the instrument, B_ℓ the beam of the instrument, $a_{\ell m}^{\text{obs}}$ the spherical harmonic coefficient of the temperature data $d_{\text{obs}}(\hat{n})$

$$a_{\ell m}^{\text{obs}} = \int d^2\hat{n} Y_{\ell,m}^*(\hat{n}) d_{\text{obs}}(\hat{n}), \quad (\text{D4})$$

and the similar relation between $a_{\ell m}^m(\mathbf{V})$ and $d_m(\hat{n}, \mathbf{V})$. By maximising the likelihood of the bulk flow component, thus minimising the above χ^2 according to the components V^a , we obtain the following algebraic expression:

$$V^a = \sum_{b=1}^3 (\mathcal{M}^{-1})^{a,b} \mathcal{V}^b \quad (\text{D5})$$

with

$$\mathcal{M}^{a,b} = 2 \sum_{\ell,m} \frac{1}{C_\ell} \left(\int d^2\hat{r} \int_{r=0}^{R_s} dr Y_{\ell,m}^*(\hat{r}) n_e(r\hat{r}) \hat{r}^a \right) \left(\int d^2\hat{s} \int_{s=0}^{R_s} ds Y_{\ell,m}(\hat{s}) n_e(s\hat{s}) \hat{s}^b \right), \quad (\text{D6})$$

$$\mathcal{V}^a = 2 \sum_{\ell,m} \frac{1}{C_\ell} \int d^2\hat{r} d^2\hat{s} \int_{r=0}^{R_s} \int_{s=0}^{+\infty} dr ds Y_{\ell,m}^*(\hat{r}) Y_{\ell,m}(\hat{s}) n_e(r\hat{r}) n_e(s\hat{s}) \hat{r}^a \hat{s}^b v^b(s\hat{s}). \quad (\text{D7})$$

We look for the average properties of the estimator given in Eq. (D5) of the bulk flow \mathbf{V} . To do this, we want to compute the average response of the estimator for different velocity fields and for a fixed positions of tracers. Thus the densities n_e are kept constant, but the velocity field $\mathbf{v}(\mathbf{r})$ is left free. A useful tool to quantify the averaging properties

is to consider the covariance $\langle V^a V^b \rangle$. Through $\mathcal{M}^{a,b}$, it is directly related to $\langle \mathcal{V}^a \mathcal{V}^b \rangle$:

$$\begin{aligned} \langle \mathcal{V}^a \mathcal{V}^b \rangle = & 4 \sum_{\ell, m} \sum_{\ell', m'} \frac{1}{C_\ell C_{\ell'}} \int d^2 \hat{r} d^2 \hat{s} d^2 \hat{r}' d^2 \hat{s}' \int_{r=0}^{R_S} \int_{s=0}^{+\infty} \int_{r'=0}^{R_S} \int_{s'=0}^{+\infty} dr ds Y_{\ell, m}^*(\hat{r}) Y_{\ell, m}(\hat{s}) Y_{\ell', m'}^*(\hat{r}') Y_{\ell', m'}(\hat{s}') \\ & \times n_e(\mathbf{r}) n_e(\mathbf{s}) n_e(\mathbf{r}') n_e(\mathbf{s}') \hat{r}^a \hat{r}'^b \hat{s}^c \hat{s}'^d \langle v^c(\mathbf{s}) v^d(\mathbf{s}') \rangle. \end{aligned} \quad (\text{D8})$$

Assuming that the linear perturbation theory is a good description of the velocity field, that the statistics of density fluctuations is purely Gaussian and described by a power spectrum $P(k)$, then the covariance of the velocity field is

$$\langle v^c(\mathbf{s}) v^d(\mathbf{s}') \rangle = \frac{a^2 H^2 f^2}{2\pi^2} \int_{k=0}^{+\infty} dk P(k) \int d^2 \hat{k} \hat{k}^c \hat{k}^d e^{ik\hat{k} \cdot (\mathbf{s} - \mathbf{s}')}, \quad (\text{D9})$$

with $f = d \log D / d \log a$, D the growth factor, a the scale factor of the Universe and H the Hubble constant. We may now rewrite Eq. (D8)

$$\langle \mathcal{V}^a \mathcal{V}^b \rangle = a^2 H^2 f^2 \int_{k=0}^{+\infty} \frac{dk}{6\pi^2} P(k) \widetilde{\mathcal{W}}^{a,b}(k), \quad (\text{D10})$$

with

$$\begin{aligned} \widetilde{\mathcal{W}}^{a,b}(k) = & 4 \sum_{\ell, m} \sum_{\ell', m'} \frac{1}{C_\ell C_{\ell'}} \int d^2 \hat{r} d^2 \hat{s} d^2 \hat{r}' d^2 \hat{s}' \int_{r=0}^{R_S} \int_{s=0}^{+\infty} \int_{r'=0}^{R_S} \int_{s'=0}^{+\infty} dr ds Y_{\ell, m}^*(\hat{r}) Y_{\ell, m}(\hat{s}) Y_{\ell', m'}^*(\hat{r}') Y_{\ell', m'}(\hat{s}') \\ & \times n_e(\mathbf{r}) n_e(\mathbf{s}) n_e(\mathbf{r}') n_e(\mathbf{s}') \hat{r}^a \hat{r}'^b \hat{s}^c \hat{s}'^d \int \frac{3d^2 \hat{k}}{4\pi} \hat{k}^c \hat{k}^d e^{ik\hat{k} \cdot (\mathbf{s} - \mathbf{s}')}. \end{aligned} \quad (\text{D11})$$

Up to a multiplication by the inverse of $\mathcal{M}^{a,b}$, we call this function the window function of the estimator. According to Eq. (D10), this function is a transfer function to apply on the power spectrum of density fluctuations to obtain the covariance of the estimated bulk flow. $\widetilde{\mathcal{W}}^{a,b}$ indicates what are the scales probed by the estimator. Other similar window functions have been derived in the literature in the context of survey of peculiar velocities of galaxies (Watkins et al. 2009). Some factorisation may be done:

$$\widetilde{\mathcal{W}}^{a,b}(k) = 4 \sum_{\ell, m} \sum_{\ell', m'} \frac{1}{C_\ell C_{\ell'}} g_{\ell, m} g_{\ell', m'} \int_{s=0}^{+\infty} \int_{s'=0}^{+\infty} Y_{\ell, m}(\hat{s}) Y_{\ell', m'}(\hat{s}') n_e(\mathbf{s}) n_e(\mathbf{s}') \hat{s}^c \hat{s}'^d \int \frac{3d^2 \hat{k}}{4\pi} \hat{k}^c \hat{k}^d e^{ik\hat{k} \cdot (\mathbf{s} - \mathbf{s}')}. \quad (\text{D12})$$

with

$$g_{\ell, m}^a = \int d^2 \hat{n} \int_{r=0}^{R_S} dr \hat{n}^a Y_{\ell, m}^*(\hat{n}) n_e(\mathbf{r}). \quad (\text{D13})$$

$g_{\ell, m}^a$ is exactly the spherical harmonic representation of the kSZ templates that we are using to do the fitting of the component a of the bulk flow in Section 3.1. The part after the integration symbol in the Equation D12 corresponds to the complete kSZ signal generated by the whole observable universe.

The above expression is exact up to the approximation of the linear perturbation theory. To go further we have to approximate the behaviour of $n_e(\mathbf{r})$. In the following, we will make the following approximation: the galaxies have a much smaller size than the considered scales, their distances are large compared to their size, and their density profile is going to be simplified to the maximum. We consider that it can be expanded like:

$$n_e(\mathbf{r}) \simeq \sum_{i=1}^{N_{\text{galaxy}}} W(\mathbf{r} - \mathbf{x}_i), \quad (\text{D14})$$

with \mathbf{x}_i the position of the i -th galaxy. This sum runs over all galaxy of the observable Universe. W being a function with compact support, we approximate it as a small cone:

$$W(\mathbf{r} - \mathbf{x}_i) \simeq A_e H(r - x_i) \Theta_i(\hat{r}), \quad (\text{D15})$$

with $\Theta_i(\hat{r}) = 1$ if $\cos^{-1}(\hat{r} \cdot \hat{x}_i) \leq R/x_i$ and zero otherwise, and $H(r) = 1$ only if $|r| \leq R$, zero otherwise, and A_e the mean number density of electrons in the galaxy. This representation of the distribution of electrons in a galaxy is very

schematic but sufficient to derive the window function. We now replace the expression $n_e(\mathbf{r})$ in Equation (D12):

$$\widetilde{\mathcal{W}}^{a,b}(k) \simeq 4 \sum_{\ell,m} \sum_{\ell',m'} \frac{1}{C_\ell C_{\ell'}} g_{\ell,m}^a g_{\ell',m'}^b \sum_{i,j=1}^{N_{\text{galaxies}}} \left[\int_{s=0}^{+\infty} \int_{s'=0}^{+\infty} d^2 \hat{s} d^2 \hat{s}' W(\mathbf{s} - \mathbf{x}_i) W(\mathbf{s}' - \mathbf{x}_j) Y_{\ell,m}(\hat{s}) Y_{\ell',m'}(\hat{s}') \hat{s}^c \hat{s}'^d \right. \quad (\text{D16})$$

$$\left. \int \frac{3d^2 \hat{k}}{4\pi} \hat{k}^c \hat{k}^d e^{i\mathbf{k} \cdot (\mathbf{s} - \mathbf{s}')} \right], \quad (\text{D17})$$

$$= 16R^2 \sum_{\ell,m} \sum_{\ell',m'} \frac{1}{C_\ell C_{\ell'}} g_{\ell,m}^a g_{\ell',m'}^b \sum_{i,j} \int d^2 \hat{s} d^2 \hat{s}' Y_{\ell,m}(\hat{s}) Y_{\ell',m'}(\hat{s}') \hat{s}^c \hat{s}'^d \int \frac{3d^2 \hat{k}}{4\pi} \hat{k}^c \hat{k}^d h_i(\mathbf{k} \cdot \hat{s}) h_j^*(\mathbf{k} \cdot \hat{s}') \Theta_i(\hat{s}) \Theta_j(\hat{s}'), \quad (\text{D18})$$

with i and j running over the galaxies of the observable Universe, and

$$h_i(k) = \text{sinc}(kR) e^{ikx_i}. \quad (\text{D19})$$

We only consider scales much larger than the size of a galaxy, R , thus $kR \ll 1$ and $\text{sinc}(kR) \simeq 1$ to first order in kR . We find

$$\widetilde{\mathcal{W}}^{a,b}(k) = 16R^2 \sum_{\ell,m} \sum_{\ell',m'} \frac{1}{C_\ell C_{\ell'}} g_{\ell,m}^a g_{\ell',m'}^b \sum_{i,j} \int d^2 \hat{s} d^2 \hat{s}' Y_{\ell,m}(\hat{s}) Y_{\ell',m'}(\hat{s}') \hat{s}^c \hat{s}'^d \int \frac{3d^2 \hat{k}}{4\pi} \hat{k}^c \hat{k}^d \Theta_i(\hat{s}) \Theta_j(\hat{s}') e^{i\mathbf{k} \cdot (\hat{s}x_i - \hat{s}'x_j)}, \quad (\text{D20})$$

$$\simeq 16\pi^2 R^2 \sum_{i,j} \sum_{\ell,m} \sum_{\ell',m'} \frac{1}{C_\ell C_{\ell'}} g_{\ell,m}^a g_{\ell',m'}^b Y_{\ell,m}(\hat{x}_i) Y_{\ell',m'}(\hat{x}_j) \hat{x}_i^c \hat{x}_j^d \left(\frac{R^2}{x_i x_j} \right)^2 \int \frac{3d^2 \hat{k}}{4\pi} \hat{k}^c \hat{k}^d e^{i\mathbf{k} \cdot (\mathbf{x}_i - \mathbf{x}_j)} \quad (\text{D21})$$

$$= 16\pi^2 R^2 \sum_{i,j} \mathcal{T}^a(\hat{x}_i) \mathcal{T}^b(\hat{x}_j) \left(\frac{R^2}{x_i x_j} \right)^2 \hat{x}_i^c \hat{x}_j^d G^{c,d}(k(\mathbf{x}_i - \mathbf{x}_j)) \quad (\text{D22})$$

with

$$G^{a,b}(\mathbf{x}) = G_0(|\mathbf{x}|) \delta^{a,b} + G_1(|\mathbf{x}|) \hat{x}^a \hat{x}^b \quad (\text{D23})$$

$$G_0(x) = 3 \frac{\sin x - x \cos x}{x^3} \quad (\text{D24})$$

$$G_1(x) = \frac{x^2 \sin x + 3x \cos x - 3 \sin x}{x^3} \quad (\text{D25})$$

and

$$\mathcal{T}^a(\hat{n}) = \sum_{\ell,m} \frac{1}{C_\ell} g_{\ell,m}^a Y_{\ell,m}(\hat{n}). \quad (\text{D26})$$

The summation over all galaxies can effectively be truncated to the depth of the survey R_S . In Eq. (D22) the summation over the galaxies corresponds to compute the cross correlation between the weighted templates \mathcal{T}^a and the projected density of the Universe of the sky given by the other terms. This correlation small, though not negligible, whenever the galaxy i or j is outside the volume on which we are fitting. We show the amplitude of this effect in Figure D1. We note that the function is reduced at $k \gtrsim 0.1h \text{ Mpc}^{-1}$. The shape is preserved for $k \lesssim 0.1h \text{ Mpc}^{-1}$.

We note that the derived window function cannot be trusted on scales $k \gtrsim 1/R$. The reason lies in the simplistic assumption on the density profiles and the approximation on the expansion of the function sinc.

The last missing piece consists in deriving the covariance matrix $\mathcal{M}^{a,b}$. As we have used an approximation for only one part of the derivation of the unweighted window function $\widetilde{\mathcal{W}}^{a,b}$, we ought to do the same for the derivation of $\mathcal{M}^{a,b}$ even though it is not required. The covariance matrix becomes:

$$\mathcal{M}^{a,b} = 2 \sum_{\ell,m} \frac{1}{C_\ell} g_{\ell,m}^a \left(\int d^2 \hat{s} \int_{s=0}^{R_S} ds Y_{\ell,m}(\hat{s}) n_e(s\hat{s}) \hat{s}^b \right) \quad (\text{D27})$$

$$\simeq 4\pi R \sum_{i, x_i \leq R_S} \sum_{\ell,m} \frac{1}{C_\ell} g_{\ell,m}^a \left(\frac{R}{x_i} \right)^2 Y_{\ell,m}(\hat{x}_i) \hat{x}_i^b \quad (\text{D28})$$

$$= 4\pi R \sum_{i, x_i \leq R_S} \mathcal{T}^a(\hat{x}_i) \left(\frac{R}{x_i} \right)^2 \hat{x}_i^b, \quad (\text{D29})$$

with the summation is limited to galaxies with $x_i \leq R_S$ as indicated by $i/x_i \leq R_S$. We note that we lose the obvious symmetry of $\mathcal{M}^{a,b}$ by making this approximation. Using the expression (D29), we note that

$$\widetilde{\mathcal{W}}^{a,b}(k=0) = \sum_{c=1}^3 \mathcal{M}^{a,c} \mathcal{M}^{c,b}. \quad (\text{D30})$$

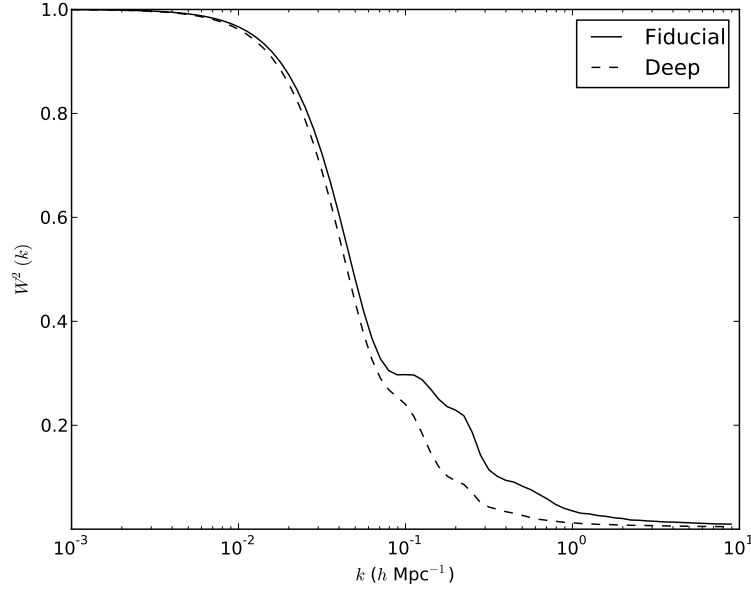


Figure D1. We show the problem of the convergence of the window function for $\mathcal{W}^{x,x}(k)$. The fiducial curve corresponds to taking the same sample for the galaxies $\{\mathbf{x}_i\}$ in Equation (D22) as for the computation of the base template \mathcal{T}^a , in this case $50h^{-1}$ Mpc. The deep curve is obtained by considering a sample of galaxies twice deeper for galaxies \mathbf{x}_i , thus $100h^{-1}$ Mpc, than for deriving \mathcal{T}^a .

Consequently the weighted window function $\mathcal{W}^{a,b}(k)$, defined through the covariance

$$\langle V^a V^b \rangle = a^2 H^2 f^2 \int_{k=0} \frac{dk}{6\pi^2} P(k) \mathcal{W}^{a,b}(k) = \sum_{c,d=1}^3 (\mathcal{M}^{-1})^{a,c} (\mathcal{M}^{-1})^{d,b} \langle \mathcal{V}^c \mathcal{V}^d \rangle \quad (\text{D31})$$

is related to $\widetilde{\mathcal{W}}^{a,b}$ through:

$$\mathcal{W}^{a,b}(k) = \sum_{c,d=1}^3 (\mathcal{M}^{-1})^{a,c} (\mathcal{M}^{-1})^{d,b} \widetilde{\mathcal{W}}^{c,d}(k). \quad (\text{D32})$$

We conclude by acknowledging that $\mathcal{W}^{a,b}(k=0) = \delta^{a,b}$.

APPENDIX E: NUMERICAL TEST ON MOCK SKY MAPS

We have checked using mock sky maps our numerical implementation of our template matching likelihood of Section 2. We have generated mock sky maps using the best fit value for our model which are given in the Tables 3 (line one) and 5 (line one). We have used the best fit value obtained using WMAP7 data for the parameters of the Λ CDM model. We have generated randomly the phases of the primary CMB fluctuations. All the components (tSZ, kSZ, point sources, galaxy foreground contamination, CMB) have then been summed, smoothed using the beam transfer function provided by the WMAP collaboration for the 7-year data. In the end, we have added a random noise, uncorrelated in pixel space, and weighed according to the number of observations. We produce in such a way one mock sky map per frequency channel (Q, V and W). The primary CMB is kept exactly the same between sky maps but the noise is independent. We show in Figure E1 the final mock sky map that we have obtained for the W channel.

Table E1 gives the input value that we have used to generate the mock sky maps, then the best-fitted value with their attach predicted error bars by the Bayesian analysis for one mock sky map. Most of the fitted values are in agreement with the input value within the 2σ range. The exception being the fitted values of the foreground $T_K - T_{K_A}$ which are at 2.5σ from the input value. Finally in Figure E2, we show the distribution for the mean of the X-component of the kSZ bulk flow for 100 mock-sky. The distribution is centered on the actual input value that we have chosen and normalised by the standard deviation predicted by our algorithm. We have overplotted, with a thick solid red line, the expected distribution for these values, which is a Gaussian distribution centered on zero with unit variance. During the tests, we have also noted a small numerical bias in the computation of the amplitude of the tSZ template. At the level of present error bars, this is not significant ($\sim 0.2 - 0.5\sigma$) and it can be significantly reduced by increasing the resolution of the maps. We thus conclude that our implementation of the statistical method given in Section 2 works as advertised, and provided the models are correct, is unbiased.

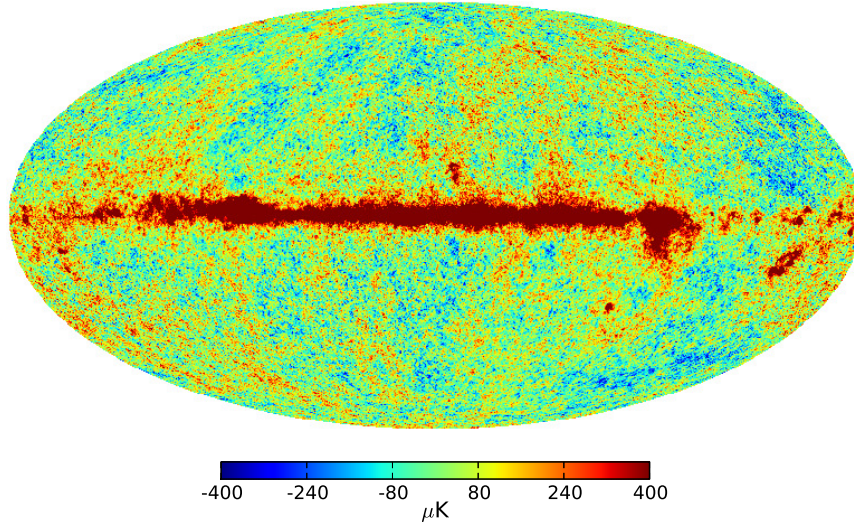


Figure E1. Mock CMB sky map generated as indicated in Appendix E. We show the mock sky map obtained in the W band, at $N_{\text{side}} = 512$, assuming the characterization of the statistical properties of the map given by the WMAP collaboration and our best fit value for the templates that we have adopted.

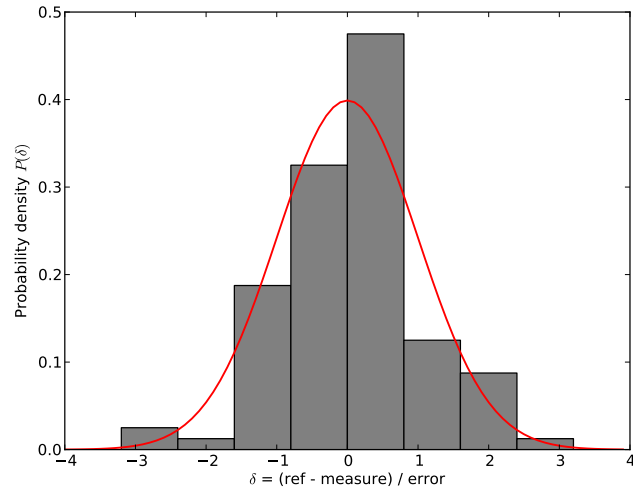


Figure E2. Example of the full posterior of the X component of the kSZ bulk flow signal detected in 100 simulations mimicking WMAP maps characteristics, as explained in Section E. The histograms are derived from binning the results of the mock measurements on simulations, after normalization by the predicted standard deviation. The red solid curve is the expected Gaussian curve, with unit variance.

Parameter	Frequency channel	Input value	Posterior value
Monopole	Q	0.40 mK	0.46 ± 0.03 mK
	V	0.19 mK	0.25 ± 0.03 mK
	W	0.11 mK	0.17 ± 0.03 mK
Dipole (1,0)	Q	10 μ K	12.4 ± 1.6 μ K
	V	9 μ K	11.5 ± 1.6 μ K
	W	1 μ K	3.60 ± 1.60 μ K
Dipole (1,1)	Q	$(-0.3 - 6i)$ μ K	$(6 \pm 7) - (3 \pm 5)i$ μ K
	V	$(0.2 - 4i)$ μ K	$(6 \pm 7) - (0.4 \pm 5)i$ μ K
	W	$(0.4 - 6i)$ μ K	$(6 \pm 7) - (2 \pm 5)i$ μ K
H_α	Q	1.5 μ K R $^{-1}$	2.2 ± 0.4 μ K R $^{-1}$
	V	1.0 μ K R $^{-1}$	1.7 ± 0.4 μ K R $^{-1}$
	W	0.7 μ K R $^{-1}$	1.4 ± 0.4 μ K R $^{-1}$
Dust	Q	0.1	-0.3 ± 0.3
	V	0.3	-0.1 ± 0.3
	W	1.0	0.6 ± 0.3
$T_K - T_{K_A}$	Q	0.37	0.42 ± 0.02
	V	0.18	0.23 ± 0.02
	W	0.11	0.16 ± 0.02
PSC	Q	60 μ Jy	60 ± 20 μ Jy
	V	120 μ Jy	80 ± 60 μ Jy
	W	400 μ Jy	500 ± 300 μ Jy
tSZ		1.0	0.93 ± 0.12
kSZ V_x		559 km s $^{-1}$	462 ± 267 km s $^{-1}$
kSZ V_y		-412 km s $^{-1}$	-431 ± 286 km s $^{-1}$
kSZ V_z		-93 km s $^{-1}$	-76 ± 187 km s $^{-1}$

Table E1. Result of the test on a single mock-sky realization.

NOTE: We have used some fiducial realistic values for the model mentioned in the table. These values are derived from best-fitting the models on WMAP data. The posterior values is derived from the mean and standard deviation as provided by the posterior distribution.